Kinesin-4 KIF21B limits microtubule growth to allow rapid centrosome polarization in T cells

Peter Jan Hooikaas[1]*, Hugo G.J. Damstra[1]*, Oane J. Gros[1], Wilhelmina E. van Riel[1,2], Maud Martin[1,3], Yesper T.H. Smits[4], Jorg van Loosdregt[4], Lukas C. Kapitein[1], Florian Berger[1 &] and Anna Akhmanova[1&]

[1] Cell Biology, Neurobiology and Biophysics, Department of Biology, Faculty of Science, Utrecht University, Utrecht, Netherlands.

[2] Current address: Netherlands Translational Research Center B.V., Kloosterstraat 9, 5349 AB Oss.

[3] Current address: Laboratory of Neurovascular Signaling, Department of Molecular Biology, Université libre de Bruxelles (ULB), B-6041 Gosselies, Belgium.

[4] Center for Translational Immunology, University Medical Center Utrecht, Utrecht University, Utrecht, Netherlands.

* These authors contributed equally to this work

[&] Corresponding authors: a.akhmanova@uu.nl; f.m.berger@uu.nl

Abstract

When a T cell and an antigen-presenting cell form an immunological synapse, rapid dynein-driven translocation of the centrosome towards the contact site leads to reorganization of microtubules and associated organelles. Currently, little is known about how the regulation of microtubule dynamics contributes to this process. Here, we show that the knockout of KIF21B, a kinesin-4 linked to autoimmune disorders, causes microtubule overgrowth and perturbs centrosome translocation. KIF21B restricts microtubule length by inducing microtubule pausing typically followed by catastrophe. Catastrophe induction with vinblastine prevented microtubule overgrowth and was sufficient to rescue centrosome polarization in KIF21B-knockout cells. Biophysical simulations showed that a relatively small number of KIF21B molecules can restrict microtubule length and promote an imbalance of dynein-mediated pulling forces that allows the centrosome to translocate past the nucleus. We conclude that proper control of microtubule length is important for allowing rapid remodeling of the cytoskeleton and efficient T cell polarization.

Introduction

Large-scale reorganization of the microtubule (MT) cytoskeleton is essential for a variety of processes, such as cell division, differentiation and polarization. In dividing cells, a balance of dynein-dependent pulling forces and MT pushing forces determines the positioning of the MT-based mitotic spindle (Howard and Garzon-Coral, 2017; Kotak and Gonczy, 2013). In interphase cells with dense, non-centrosomal MT arrays, such as epithelial or neuronal cells, polarization is a slow process that requires hours, if not days (reviewed in (Kapitein and Hoogenraad, 2015; Meiring et al., 2020)). In contrast, interphase cells with sparse centrosome-based networks can rapidly switch polarity and reposition their MTs. For example, when a T cell encounters an antigen-presenting cell (APC), it translocates its centrosome and associated MTs towards the APC-contact side (Geiger et al., 1982; Kupfer et al., 1983; Stinchcombe et al., 2006; Yi et al., 2013) and forms an immunological synapse (reviewed in (Dustin et al., 2010)), a highly specialized compartment encircled by an actin-rich ring. The immunological synapse facilitates T-cell signaling and polarized secretion of cytokines or lytic molecules towards the APC (Figure 1A). The process of centrosome repositioning takes only a few minutes and is driven by membrane-associated dynein that pulls MTs with the attached centrosome towards the synapse (Combs et al., 2006; Liu et al., 2013a; Martin-Cofreces et al., 2008; Nath et al., 2016).

Whereas the role of dynein as force generator in centrosome translocation in T cells is firmly established, little is known about the properties of the MT network and MT dynamics that facilitate this rapid cytoskeletal reorganization, and only a few MT regulators participating in this process have been identified. Among them, MT-associated protein MAP4 was shown to be required for centrosome translocation (Bustos-Moran et al., 2017), potentially due its ability to regulate dynein (Samora et al., 2011; Semenova et al., 2014; Seo et al., 2016). In addition, both acetylation and detyrosination of MTs and a complex of casein kinase Iδ with EB1 were suggested to be important for efficient centrosome polarization (Andres-Delgado et al., 2012; Serrador et al., 2004; Zyss et al., 2011). Finally, a study describing the knockout of stathmin/OP18, a MT-destabilizing protein, in mouse cytotoxic T cells showed decreased centrosome polarization efficiency (Filbert et al., 2012). Yet, how these cytoskeletal perturbations affect the MT network of T cells as a whole and how this would consequently hinder centrosome translocation is poorly understood.

An interesting candidate to regulate MT dynamics in immune cells is kinesin-4 KIF21B. Kinesin-4 family members are well known for their ability to limit MT growth in a variety of

cellular processes (Bieling et al., 2010; Bringmann et al., 2004; He et al., 2014; Yue et al., 2018). Among them are two closely related motors KIF21A and KIF21B, which consist of an N-terminal motor domain, several coiled-coil regions and a C-terminal WD40 domain (Marszalek et al., 1999). KIF21A is expressed in many tissues; it is well studied because point mutations impairing its auto-inhibition lead to congenital fibrosis of the extraocular muscles type 1 (CFEOM1), a neurodevelopmental disorder that affects eye movement (Bianchi et al., 2016; Cheng et al., 2014; Traboulsi and Engle, 2004; van der Vaart et al., 2013; Yamada et al., 2003). *In vitro*, KIF21A slows down MT growth and suppresses catastrophes, whereas in cells it prevents overgrowth of MTs at the cell cortex (van der Vaart et al., 2013).

KIF21B is expressed in brain, eyes and spleen (Marszalek et al., 1999). Several studies have linked the *KIF21B* gene to neurodevelopmental and immune-related disorders, including multiple sclerosis and inflammatory conditions such as Crohn's disease and ankylosing spondylitis (Anderson et al., 2009; Asselin et al., 2020; Barrett et al., 2008; Garcia-Etxebarria et al., 2016; Goris et al., 2010; International Multiple Sclerosis Genetics, 2010; Kannan et al., 2017; Kreft et al., 2014; Li et al., 2017; Liu et al., 2013b; Robinson et al., 2015; Yang et al., 2015). *Kif21b* knock out mice are viable but show behavioral deficits and defects in synaptic transmission (Ghiretti et al., 2016; Gromova et al., 2018; Morikawa et al., 2018; Muhia et al., 2016). At the cellular level, KIF21B has been reported to be a processive kinesin involved in neuronal transport (Ghiretti et al., 2016; Gromova et al., 2018; Labonte et al., 2014) and Rac1 inactivation (Morikawa et al., 2018). Furthermore, similar to all other kinesin-4 family members, KIF21B acts as a MT growth regulator both *in vitro* and in cells (Ghiretti et al., 2016; Muhia et al., 2016; van Riel et al., 2017). However, the activity of this kinesin is a matter of controversy, because one study reported that it acts as a positive regulator of MT dynamicity by increasing MT growth rate and catastrophe frequency; in these assays, KIF21B was present at relatively high concentrations (50-300 nM) and was mainly observed to bind to depolymerizing MT ends and lattices (Ghiretti et al., 2016). In contrast, our own work showed that KIF21B walks to MT plus ends where it slows down MT growth and potently induces MT pausing already at low nanomolar concentrations, with only one or two KIF21B molecules being sufficient to block elongation of a MT plus end (van Riel et al., 2017). Somewhat conflicting results have also been reported on the effects of the loss of KIF21B on MT plus end growth in neurons: two different studies found opposite effects on MT growth rates, although they agreed that KIF21B reduces MT growth processivity (Ghiretti et al., 2016; Muhia et al.,

2016). Therefore, further analyses of KIF21B behavior and function are required to elucidate its role in regulating MT dynamics.

Here, we have investigated the role of KIF21B in regulating MT organization and dynamics in T cells. We generated KIF21B knockout (KIF21B-KO) Jurkat T cell lines, which displayed defects during immunological synapse formation, particularly in translocating their centrosome towards the synapse. These defects were rescued by KIF21B-GFP re-expression, and live-cell imaging of single KIF21B-GFP motors showed that they walked to MT plus ends and often induced MT pausing followed by depolymerization, very similar to our previous *in vitro* observations (van Riel et al., 2017). Using expansion microscopy, we visualized three-dimensional MT organization in Jurkat T cells and found that MTs were longer in KIF21B-KO cells. Interestingly, we could rescue centrosome polarization defects in KIF21B-KO cells by mildly increasing MT catastrophe frequency with a low dose of vinblastine, a MT-depolymerizing drug. These results were recapitulated in a two-dimensional computational model demonstrating that long MTs impaired centrosome polarization by altering the balance of dynein-drive pulling forcing in a way that prevents symmetry breaking, which could be restored by introducing more frequent catastrophes that limit MT length. We conclude that proper control of MT growth plays a critical role in T cell polarization.

Results

KIF21B knockout T cells are defective in centrosome polarization after activation

To study MT reorganization during immune synapse formation, we used Jurkat T lymphocyte cells. We mimicked *in vivo* T-cell activation by exposing these cells to anti-CD3 coated surfaces, as described previously (Bunnell et al., 2001; Parsey and Lewis, 1993)(Figure 1A,B). We confirmed KIF21B protein expression in these cells by Western blotting (Figure 1C, Figure 1 – figure supplement 1). Using CRISPR/Cas9 technology we generated KIF21B knockout cells and selected two clones (#1 and #2) that were analyzed further. To perform rescue experiments, these two knockout cell lines were infected with a lentivirus expressing full-length KIF21B-GFP and the obtained polyclonal cell lines were sorted for GFP-positive cells and analyzed by Western blotting (Figure 1C, Figure 1 – figure supplement 1). KIF21B expression was lost in both knockout lines, whereas KIF21B-GFP expression mildly exceeded endogenous KIF21B. Expression of α-tubulin was not affected in these lines. In addition, we established that these Jurkat T cell lines were responsive to stimulus by first confirming the presence of CD3ε, a subunit of the T cell receptor (TCR) (Figure 1C, Figure 1 – figure supplement 1). Next, we stimulated control and KIF21B-KO cells with phorbol 12-myristate 13-acetate (PMA) and ionomycin, which increase the downstream intermediates of TCR signaling, protein kinase C activity and intracellular calcium levels, respectively. This stimulation regime upregulates Interleukin-2 (IL-2) mRNA expression, a hallmark of T cell activation, and we found that our knockout cell lines responded similarly to control cells (Figure 1 – figure supplement 2A,B).

To monitor immunological synapse formation, we added Jurkat cells to anti-CD3 coated coverslips, fixed the cells 10 min later and stained them with phalloidin to visualize the peripheral actin ring (Figure 1B, D). We measured synapse size and noticed that KIF21B-KO cell lines formed 28.4% (KO #1) and 27.3% (KO #2) smaller synapses compared to control cells and that this phenotype could be partially rescued by re-expression of KIF21B-GFP (Figure 1E). The reduction in the size of immunological synapses in KIF21B-KO cells was not due to smaller overall size of these cells, as their volume was the same as that of control cells (Figure 1 – figure supplement 2C,D). Live-cell imaging using Differential Interference Contrast (DIC) microscopy showed that synapse formation was slower in KIF21B-KO cells (Figure 1 – figure supplement 2E-G).

Next, we analyzed the overall MT organization in these cells by Total Internal Reflection Fluorescence (TIRF) microscopy, which visualizes a thin optical section located

above the coverslip. In fully polarized cells, the centrosome-centered MT aster was visible in the TIRF focal plane, whereas in cells that failed to polarize properly, the centrosome was not visible by TIRF, and MTs located in the vicinity of the coverslip appeared disorganized (Figure 1F). In this experiment, the centrosome was located in the plane of the synapse in the majority of control (76%) and KIF21B-GFP expressing cells (74.3 and 63.3%), whereas this was the case only in 45.5% (KO #1) and 43.6% (KO #2) of KIF21B-KO cells (Figure 1G).

During T cell activation, lysosomes cluster around the centrosome and relocate together with it towards the synapse (Figure 1A, B). Immunostaining of non-activated Jurkat cells on poly-D-lysine coated coverslips showed that lysosomes were scattered throughout the cytoplasm. We note that although it has been reported that cationic surfaces are sufficient to initiate T cell signaling (Santos et al., 2018), in our hands, exposure to poly-D-lysine-coated coverslips did not trigger centrosome polarization or lysosome clustering (Figure 1H, Figure 1 - figure supplement 2H,I). In contrast, after, activation on anti-CD3 coated coverslips, both control and knockout cells showed lysosome clustering, indicating that KIF21B knockout does not affect the minus-end directed transport of lysosomes (Figure 1H, I). We then analyzed the position of the lysosome cluster relative to the coverslip using z-projections of these cells and found that only 52.4% KIF21B-KO #1 and 50.4% KIF21B-KO #2 cells contained a polarized lysosome cluster compared to 71% in control cells (Figure 1I, J). Again, we could rescue this phenotype by re-expressing KIF21B-GFP (Figure 1J, K). These data suggest that KIF21B-KO Jurkat cells exhibit defects in immunological synapse formation: they are less efficient in polarizing their centrosome and the associated lysosomes.

MT organization is altered in KIF21B knockout T cells

We next examined the organization of the MT network of control and KIF21B-KO T cells in more detail using Stimulated Emission Depletion (STED) microscopy. For optimal labelling of MTs, cells were added to anti-CD3 coated coverslips for 7 min followed by pre-permeabilization, cytoplasm extraction and fixation as described before (Tas et al., 2018). To compare MT organization in the presence or absence of KIF21B we focused on fully polarized cells, despite centrosome polarization often being impaired in KIF21B-KO cells (Figure 1F, G). We found that while in control cells most MTs were organized in an aster-like pattern, the knockout cells often contained circular MT bundles at the cell periphery. To analyze this phenotype, we made use of a custom-developed ImageJ plugin (Martin et al., 2018) to separate

our images into radial and non-radial components based on MT orientation in relation to the centrosome (Figure 2B). This analysis showed that KIF21B-KO cells have an increased proportion of non-radially oriented MTs, which are organized into peripheral MT bundles at the immunological synapse (Figure 2A-C).

To analyze whether the MT network as a whole is affected by KIF21B depletion, we used Expansion Microscopy (ExM) to visualize the complete MT network and distinguish single MT polymers in 3D. With ExM, samples are physically magnified by embedding fixed cells in a isotropically swellable polymer, giving an approximate 4.5x-fold increase in resolution in x, y, and z (Chen et al., 2015; Jurriens et al., 2020). To understand how the state of the MT network before T cell activation may affect centrosome translocation, we looked at the very early stage of immunological synapse formation. T cells were fixed after 2 min of activation, when the majority of control cells did not yet fully polarize. We noticed that the MT network appeared to be denser in KIF21B-KO cells compared to control cells (Figure 2D,E, Video 1-3). To exclude that this was caused by increased levels of MT nucleation, we counted the number of MTs originating from the centrosome by analyzing the number of filaments passing through a 1 µm thick spherical shell with an inner radius of 5 µm generated around the centrosome (Figure 2D, Video 1-3). We found that MT number was slightly reduced in KIF21B-KO cells, by 21.7% in KO #1 and 19% in KO #2 (Figure 2F). Since T cells have highly centrosome-focused MT arrays, we assumed that all MTs are anchored to the centrosome and that these numbers thus represent the total number of MTs per cell. Next, we estimated an average MT length per cell. We generated surface masks based on the colocalization of the MTs and the 1 µm-thick spherical shell around the centrosome (Fig 2D, red surfaces). Since MTs cross through the shell orthogonally to its surface, the mean intensity corresponding to 1 µm MT was determined by averaging the fluorescence intensity per surface adjusted for the number of MTs in each surface. We then used a surface mask to determine the total fluorescence intensity corresponding to the complete MT network and divided it by the MT intensity per micron and by the number of MTs. We found that KIF21B-KO cells contain fewer MTs but they are on average longer than those in control cells (Figure 2E-G). Since the overall MT mass is higher in KIF21B-KO cells (Figure 2 – figure supplement 1A,B), the concentration of free tubulin in these cells might be lower; this would affect MT nucleation at the centrosome, causing a reduction in MT number.

We furthermore examined the geometry of MTs in polarizing control and KIF21B-KO cells (Figure 2 – figure supplement 1B). Considering the immunological synapse as the basal

side of the cell, with nucleus located above it, the centrosome could be positioned on top or on the side of the nucleus, or between the nucleus and the synapse. In agreement with the previously described observations (Yi et al., 2013), a MT bundle directed from the centrosome to the synapse ("stalk") could be found in some cells (Figure 2 – figure supplement 1C). We note that it was not obvious from our images that all MTs in such a stalk terminated at synapse; rather it appeared that many of them made side contacts with the membrane. In other cases, a single basally directed MT bundle could not be distinguished (Figure 2 – figure supplement 1B), possibly because these cells were at an earlier stage of centrosome polarization. In cells with apically located centrosomes, MTs appeared to embrace the nucleus from all sides and then make lateral contacts with the synapse surface. In KIF21B-KO cells, such MTs formed a dense network in the basal half of the cell (Figure 2 – figure supplement 1B).

To summarize, T cells that lack KIF21B show MT overgrowth at the immunological synapse. Using 3D ExM, we confirmed this observation and showed that KIF21B-KO cells have overly long MTs that form dense arrays at the immunological synapse.

KIF21B is a processive motor that induces MT pausing and catastrophes

Next, we investigated the localization and dynamics of KIF21B by live-cell imaging of the KIF21B-KO cell line rescued by re-expressing KIF21B-GFP. In HeLa cells, the closely related paralogue KIF21A displays strong peripheral localization at cortical MT stabilizing complexes (CMSC), to which it binds through KANK proteins (Noordstra and Akhmanova, 2017; van der Vaart et al., 2013). Structural studies have elucidated the binding interface of this interaction, and it is clear that KIF21B does not possess the KANK-binding region required for association with the CMSC (Guo et al., 2018; Pan et al., 2018; Weng et al., 2018). Likewise, KIF21B-GFP did not show any obvious cortical accumulation in T cells but was rather diffusely distributed in the cytoplasm or associated to MTs on which it moved processively (Figure 3A, Video 4). The average velocity of KIF21B-GFP puncta was 0.77 ± 0.14 µm/s (mean ± SD) (Figure 3A,B), which is 1.2 and almost 4 times faster compared to velocities measured for the full-length motor in COS-7 cells and hippocampal neurons, respectively (Ghiretti et al., 2016; van Riel et al., 2017).

To investigate whether the observed KIF21B-GFP signals correspond to single kinesin dimers, we compared their fluorescence intensity to that of single GFP molecules, as described previously for *in vitro* reconstitution assays (Aher et al., 2018; Hooikaas et al., 2019; van Riel

et al., 2017). We imaged dual chamber slides that contained purified monomeric GFP in one chamber and activated KIF21B-GFP-expressing T cells in the other chamber. Intracellular KIF21B-GFP motors were detected using DoM software (see Methods for details) and the detected signals were filtered for molecules belonging to tracks ≥ 1 s (Figure 3 - figure supplement 1A). We found that their signal was ~1.5 times brighter than that of monomeric GFP (Figure 3C, Figure 3 - figure supplement 1B). Given that the evanescent field used for excitation decays exponentially and the KIF21B-GFP motors observed were localized intracellularly, one should take into account the distance between the coverslip and fluorescent molecules. Although we could not measure this distance precisely, we assumed that the thickness of the plasma membrane, cortical actin, cytoplasm and the 25 nm width of a MT would result, on average, in at least 50 nm spacing. Given the penetration depth *d* in these imaged cells was calibrated at 180 nm, we estimated that the corrected the KIF21B-GFP fluorescence signal intensity was ~ 2 times brighter than that of monomeric GFP (~1.8 times assuming 50 nm distance from the coverslip or ~2.1 times assuming 75 nm distance) (Figure 3C, Figure 3 - figure supplement 1B). Most of the motile KIF21B-GFP puncta in Jurkat cells thus likely corresponded to single kinesin dimers, which did not form any clear accumulations.

Our previous *in vitro* work showed that single KIF21B molecules walked towards a growing plus end and induced transient pauses ultimately followed by a catastrophe, whereas multiple KIF21B molecules accumulated at a MT plus end induced prolonged pauses (van Riel et al., 2017). Consequently, we asked whether KIF21B behaves similarly in T cells to regulate MT dynamics. To observe the interactions of KIF21B-GFP with MT plus ends in Jurkat cells, we transfected them with EB3-mCherry, which labels growing MT ends and shows some MT lattice decoration, and imaged these cells on a TIRF microscope. We traced processive KIF21B-GFP motors and quantified events where the motor reached the tip of an EB3-mCherry comet. Most of KIF21B-GFP molecules (56.7%) transitioned to a paused state upon reaching the plus end; some motors (29.5%) dissociated from the MT and in a few cases KIF21B tracked the MT tip and then either transitioned to a paused state (9.8%) or dissociated from the MT (4%) (Figure 3D-G). It should be noted that even in cases where KIF21B motor rapidly dissociated from the MT tip, we sometimes could observe a reduction in EB3 comet intensity (Figure 3F), suggesting a transient MT growth perturbation. A pausing KIF21B-GFP motor typically did affect MT plus end growth, and the events where a MT first paused and ultimately switched to depolymerization were most frequent (55.7%). In other cases, a MT first paused but then switched back to growth after the paused KIF21B-GFP motor dissociated from the plus end

(19.5%). In a few cases (9.4%), a growing plus end kept growing after a KIF21B-GFP motor transitioned to pausing; often, such events coincided with a reduced EB3 comet intensity (Figure 3D,G,H). On average, KIF21B-GFP motors were paused for 3.0 ± 2.7 s (mean ± SD) (Figure 3I), whereas MT plus end pause durations measured with EB3-mCherry were somewhat longer, 4.2 ± 4.4 s (mean ± SD) (Figure 3I). This can be explained either by photobleaching of the GFP or by participation of additional cellular factors that could stabilize paused MT ends after KIF21B dissociates. In some cases, growing MT plus end appeared to be static; these events likely corresponded to MTs growing against an obstacle, where MT tip remained stationary while the growing MT shaft buckled and formed a loop (Figure 3 - figure supplement 1C,D). Events where KIF21B-GFP directly dissociated from a MT end upon arrival affected the growing MT plus end much less compared to KIF21B-GFP pausing events; only a few of such events coincided with the initiation of a MT pause or a direct catastrophe event (Figure 3 - figure supplement 1E,F). All these data represent events where KIF21B-GFP was observed to arrive to the MT tip by walking along the MT shaft. We also occasionally observed events where KIF21B-GFP directly bound to the MT plus end and affected MT growth, but such events were infrequent and were therefore were not quantified (Figure 3 - figure supplement 1G). We conclude that KIF21B is a fast and processive kinesin in T cells and that its activity at the plus ends limits growth by inducing MT pausing and catastrophes.

MTs grow faster and more processively in cells lacking KIF21B

Since we directly observed MT growth perturbation by KIF21B-GFP, we next set out to perform a more global analysis of MT plus-end dynamics in Jurkat cells either expressing or lacking this motor. To this end, we used lentiviral transduction to introduce EB3-GFP as a MT plus-end marker into control and KIF21B-KO cell lines. We used these cells for live imaging of growing MT plus ends in cells that were polarized after activation (Figure 4A). We found that the MT growth rate was on average increased by 18% (KO #1) and 15% (KO #2) compared to control Jurkat cells (Figure 4A, B). These observations were in line with previous work showing that overexpression of KIF21B-GFP in COS-7 cells, which do not have endogenous KIF21B, reduced MT growth rates by ~1.5 fold (van Riel et al., 2017). These data are also consistent with the observation of increased MT growth rate after transient KIF21B depletion in neurons (Ghiretti et al., 2016), but contradict the analysis of MT growth speed in *Kif21b* knockout neurons (Muhia et al., 2016). Furthermore, we observed a decrease in MT catastrophe

rate in KIF21B knockout cells (Figure 4C), which fits well with previous studies in neurons (Ghiretti et al., 2016; Muhia et al., 2016).

To further evaluate MT plus-end fate in cells lacking KIF21B, we infected control and KIF21B-KO cell lines with a GFP-β-tubulin construct as a MT marker. These cells were imaged on a TIRF microscope and we quantified events where the plus end of a radially growing MT reached the cell periphery. In control cells, a small minority (9.8%) of MTs underwent a catastrophe or continued to grow by sliding along the cell cortex (Figure 4D, E). However, most MTs paused in this region (44.2%) or continued their growth and this led to MT buckling, because the MT plus end remained stationary whereas the increasingly long MT shaft was pushed backwards and formed a loop (40.9%) (Figure 4D, E). In KIF21B-KO cells, MTs displayed less pausing at the cell periphery, whereas buckling became more frequent (Figure 4E). A closer examination of MT pauses revealed that these events in control cells were significantly more long-lived: 8.3 ± 5.6 s (mean ± SD) compared to those in KIF21B-KO cells: 4.1 ± 2.2 s (KO #1, mean ± SD) and 4.3 ± 2.4 s (KO #2, mean ± SD) (Figure 4F, Figure 4 - figure supplement 1A). We note that these pause durations are longer than those observed with EB3-mCherry (Fig. 3I), because the latter labels growing MTs, and its signal is gradually lost when MT plus ends switch to pausing and lose the GTP cap that EB3 labels (Roostalu et al., 2020). Overall, these data indicate that in T cells, KIF21B acts as a factor that inhibits MT growth and induces pausing and catastrophes.

MT growth inhibition with vinblastine rescues the defects in KIF21B knockout cells

To establish a causal connection between MT overgrowth and defects in immune synapse formation, we sought for a way to mildly inhibit MT growth in KIF21B-KO cells. Our previous work has shown that a low dose of vinblastine mildly perturbs growth and promotes catastrophes but does not induce MT depolymerization (Bouchet et al., 2016; Mohan et al., 2013). Indeed, at a low (0.5 nM) vinblastine concentration, MT network was preserved and was similar to that in control cells but different from KIF21B-KO cells, as no circular MT bundles were present at the cell periphery (compare Figure 4 –figure supplement 1B to Figure 2A). MT organization in KIF21B-KO cells treated with 0.5 nM vinblastine was similar to that of KIF21B-KO cells rescued with KIF21B-GFP (Figure 4 – figure supplement 1B). In vinblastine-treated KIF21B-KO cells, MT growth events visualized with EB3-GFP were less continuous, and the growth rates were reduced approximately to the level seen in control Jurkat cells (Figure

4A-C). We also examined the effect of 0.5 nM vinblastine on the dynamics of MTs labeled with GFP-β-tubulin and found that vinblastine application resulted in an increased catastrophe frequency, while long-lived MT pauses were not restored (Figure 4E,F, Figure 4 – figure supplement 1A).

We next tested whether such a mild vinblastine-induced MT growth inhibition would rescue the ability of the KIF21B-KO cells to polarize their centrosome. Jurkat cells were added to anti-CD3 coated coverslips and stained for CEP135, a centriole marker, to analyze polarization using z-projections (Figure 4G). We scored polarization events as successful when the centrosome was located within 2 µm from the coverslip and found that most control cells (87.2%) were polarized contrary to knockout cells (36.7 and 42.9%) (Figure 4H). This phenotype could be partially rescued by re-expressing KIF21B-GFP in these cells (58.9 and 51.7%), and an even slightly better rescue was observed after applying 0.5 nM vinblastine to both KIF21B-KO cell lines (65.4 and 66.9%) (Figure 4H, I). Altogether, we found that KIF21B depletion alters MT growth dynamics and that centrosome polarization defects in KIF21B-depleted cells can be rescued by the application of a drug, vinblastine, that inhibits MT growth. This indicates that cell polarization defects caused by the absence of KIF21B are due to its effect on MT dynamics rather than potential perturbation of transport or signaling processes.

Biophysical simulation of MT dynamics suggests that a small number of KIF21B molecules can limit MT overgrowth

To gain more insight into the regulatory effects of KIF21B and to explore possible mechanisms explaining how overly long MTs hinder centrosome polarization, we constructed a biophysical model based on *Cytosim* (Nedelec and Foethke, 2007). In contrast to previous more coarse-grained computational studies (Kim and Maly, 2009) and less modular models (Hornak and Rieger, 2020), we chose *Cytosim* to explicitly investigate the effects of KIF21B on MT dynamics. *Cytosim* uses overdamped Langevin equations to simulate the cytoskeleton with associated proteins and organelles restricted in a defined space. To model a T cell, we assumed a rotationally invariant space and simplified it to a two-dimensional object. Our model cell contains a nucleus and a centrosome, which is confined to one side of the cell and has 90 MTs attached. The cell boundary and the nucleus acted as elastic objects: when deflected, they exert a restoring force. The centrosome was modeled as a rigid sphere with uniformly spread MT anchoring points with a rotational elasticity (Figure 5A).

In our model, MTs are flexible polymers and their growth dynamics are described by two states. In the growth state, fibers elongate with a force-dependent growth speed. In the shrinkage state, fibers shorten with a constant shrinkage speed. The growth speed decreases exponentially with the force exerted on the fiber's tip, termed antagonistic force (Dogterom and Yurke, 1997). To describe the transition from growth to shrinkage, we distinguished two models: a basic 'non-pausing' model with a force-independent catastrophe rate, and a 'KIF21B-pausing' model with a force-dependent catastrophe rate (Janson et al., 2003) and KIF21B molecules that induce a paused state before the MT shrinks. To model control or KIF21B-KO cells, the number of KIF21B molecules can be changed. In our simulations, KIF21B motors freely diffuse in the cytosol, can bind to MTs and walk along them towards the plus end. When the motor arrives at a growing plus end, it pauses the MT dynamics until it unbinds. After a KIF21B motor has detached from the tip of a MT, the MT switches to the shrinkage state (Figure 5B).

To estimate numerical values for the parameters describing MT dynamics in our system, we used the experimental data for the KIF21B-KO cells (Figure 4A-F, Table S1). In this condition it is reasonable to assume that every catastrophe and pause is triggered by force exerted on the MT tip, and not by KIF21B because it is absent (Figure 5 – figure supplement 1A-D). Additionally, the KIF21B-induced mean pause time of a MT tip was set to 8.3 s, as experimentally determined (Figure 4 – figure supplement 1A). For the remaining parameters of our simulation that were unrelated to MT growth dynamics, we used numerical values found in the literature (see Table S1).

Simulations of the non-pausing model with the force-independent catastrophe rate implied that increasing the catastrophe rate decreased the mean length of the MTs (Figure 5C). The mean MT length is a measure for MT density in the simulations, as we kept the cell volume and number of MTs constant. The mean MT length reached a steady state within 300 s and decreased more than 3-fold in the range of values for the catastrophe rate we chose (Figure 5D). In the KIF21B-pausing model the fibers grew to a dense MT network in the absence of KIF21B with the force-dependent catastrophe rate matched to the KIF21B-KO (Figure 5E). When we added KIF21B motors to mimic the control condition, MT length decreased with an increasing number of KIF21B motors (Figure 5F). This decrease was approximately 2-fold between the KIF21B-KO-like and the control-like simulations between 0 and 10 KIF21B motors.

These simulations confirmed that by changing the catastrophe rate either directly or by explicitly modeling the behavior of the pause-inducing KIF21B motor, the average length of

the MTs can be regulated. Interestingly, in our simulations, a small number of KIF21B motors was sufficient to prevent the overgrowth of the MT network.

Restriction of MT length helps to avoid a force balance that inhibits polarization

To investigate how an overgrown MT network impairs centrosome polarization and whether KIF21B can rescue this defect, we extended our simulations to describe polarization. We converted our steady-state MT dynamics models to a polarizing system by releasing the centrosome confinement and initializing a 'synapse'. The synapse consists of a line with curved ends to which 50 dynein motors are attached (Figure 6A). Dynein motors are uniformly distributed over the synapse. They can bind to a MT in their vicinity and walk along them towards the centrosome. Their walking and unbinding dynamics were calculated in a force-dependent manner. Because dynein motors are anchored, walking along a MT generates a pulling force. Consequently, the centrosome is able to polarize (Figure 6B, Video 5, 6).

In both the non-pausing as well as in the KIF21B-pausing model, the cells with longer MTs needed more time on average to polarize (Figure 5D, F, 6C, D). Some KIF21B-KO-like cells without KIF21B and some cells with a fixed catastrophe rate smaller than 0.03 s^{-1} did not polarize at the end of the simulation (800 s modeled time that we simulated after the MT network reached steady state).

We next analyzed the relation between MT length and polarization dynamics in the KIF21B-pausing model, as this model describes our experimental data. Tracking the time evolution of the centrosome-synapse distance for multiple runs provided insight into the dynamics of centrosome translocation (Figure 6E). The centrosomes of late polarizing cells did not travel more slowly, but rather were localized at the far opposite side of the synapse for most of the time. Once these centrosomes left this position, they quickly moved towards the synapse. This rapid polarization movement seemed independent of the number of KIF21B molecules. However, the trapped localization before the rapid repositioning indicated that the system can be relatively stable in an unpolarized state. This state can apparently be destabilized by decreasing MT length through an increasing number of KIF21B molecules.

For our simulated cells to successfully polarize, the centrosome must travel past the nucleus on either the left or the right side. A possible explanation for the stable unpolarized state may be that the forces that dynein exerts to the left and the right are equal, thus causing a

mechanical equilibrium by force balance. To trigger polarization, this equilibrium needs to be broken. We quantified force imbalance by determining all forces exerted by dynein projected on the horizontal axis and sorting them according to their direction. We calculated the sum of forces pointing to the right and the sum of forces pointing to the left. For any timestep, the absolute difference of these two sums, normalized by the total sum of these forces indicates the force imbalance (Figure 6F, the non-normalized sum of force per timestep is shown in Figure 6 – figure supplement 1). The resulting data revealed that dynein forces were more balanced in the simulations with low KIF21B numbers and impaired polarization than in the simulations where the number of KIF21B molecules was high and polarization occurred rapidly.

To understand the underlying mechanism, we counted the number of MTs that pass the nucleus on either the right (MT_R) or the left side (MT_L) and are bound by dynein (Figure 6G). We only assessed the first 10 s after initiation of polarization to limit the situation to a period when none of the runs are already actively polarizing. This analysis indicated that with increasing number of KIF21B molecules, the mean number of MTs bound on the left or on right decreases, while the difference between the two fractions averaged over time increases. Tracking this difference as a function of time indicated that it changed together with the centrosome position, and an increased fluctuation in this number seemed necessary to trigger polarization (Figure 6H). Note that the dynamics of KIF21B together with the MTs and the spatial restriction by the nucleus can lead to enrichment of KIF21B on one side of the nucleus (Figure 6B). This specific localization could increase the difference between the number of MTs on the left and right side of the nucleus that reach the synapse and enhance the force imbalance.

We conclude that by effectively increasing catastrophe frequency and restricting MT length, KIF21B reduces the overall number of MTs reaching the synapse from different sides of the nucleus. A smaller number of long MTs leads to larger fluctuations in the number of MTs coming from opposing sides, which enables the force asymmetry that is necessary to trigger polarization when the centrosome is positioned behind the nucleus.

Discussion

In this paper, we set out to investigate which aspects of the regulation of MT organization and dynamics are important during the formation of the immunological synapse and elucidate the role of kinesin-4 KIF21B in this process. MTs are typically quite short and sparse in immune cells, and we found that this property is functionally important, as MT overgrowth inhibited efficient centrosome translocation to the synapse (Figure 7). Furthermore, our data strongly support the notion that KIF21B acts as a factor that prevents excessive MT elongation.

Previous *in vitro* studies reported contradictory results regarding the activity of KIF21B on MT ends. One study found that KIF21B promotes MT growth and catastrophe at relatively high levels (Ghiretti et al., 2016). In contrast, our own work indicated that KIF21B transiently blocks MT elongation and induces subsequent catastrophes at low levels, when only one or two KIF21B molecules are present at the MT tip, and causes prolonged MT pausing when present at a higher concentration, when multiple KIF21B motors accumulate at the plus end (van Riel et al., 2017). In the current study, we showed that the function of KIF21B in knockout cells can be rescued by KIF21B-GFP expressed at levels that were mildly exceeding endogenous. Importantly, imaging of KIF21B-GFP in these cells did not reveal any clear accumulations of the motor at MT plus ends. KIF21B behavior in Jurkat T cells was very similar to that observed at low nanomolar concentrations *in vitro* (van Riel et al., 2017): single KIF21B-GFP kinesin dimers walked processively along MTs, reached their ends and perturbed MT plus end growth by triggering transient pauses followed by catastrophes. Therefore, we conclude that whereas biochemically KIF21B can be described as a MT pausing factor, in T cells, it acts at concentrations that are insufficient to induce prolonged pausing and effectively functions as a catastrophe inducer. This is likely explained by our previous observation that a single KIF21B-GFP molecule can arrest dynamics of a few protofilaments (van Riel et al., 2017). Blocking of even one MT protofilament can already perturb growth of the remaining ones, and this can lead to the loss of the GTP cap and trigger catastrophe (Doodhi et al., 2016). To induce a pause, blocking MT elongation must be accompanied by inhibition of depolymerization of protofilaments lacking a GTP cap. Since a single KIF21B dimer is unlikely to be able to stably block depolymerization of all MT protofilaments, a catastrophe eventually ensues.

While KIF21B is a potent MT regulator, it has also been implicated in other functions, such as MT-based transport and regulation of signaling (Ghiretti et al., 2016; Gromova et al., 2018; Labonte et al., 2014; Morikawa et al., 2018). While our study certainly does not exclude that KIF21B engages in such functions in T cells, we show that centrosome polarization defects

observed in KIF21B knockout cells can be rescued by mildly perturbing MT growth with a MT-destabilizing drug. These data strongly suggest that the primary defect induced by the lack of KIF21B is excessive MT elongation. These data also argue against direct participation of KIF21B in dynein-driven capture and shrinkage of MT ends that was proposed to drive centrosome movement in T cells (Yi et al., 2013), although they do not exclude indirect effects of overly long MTs on this process. Furthermore, since KIF21B is a highly processive motor, it can be expected that it would target longer MTs more effectively, like it has been previously shown for kinesin-8 (Gupta et al., 2006; Varga et al., 2006). This would make KIF21B even more efficient in preventing excessive MT growth in T cells. The finding that KIF21B acts as an inhibitor of MT growth is in agreement with the studies in neurons, which showed that KIF21B reduces MT growth processivity (Ghiretti et al., 2016; Muhia et al., 2016).

To further substantiate the idea that KIF21B affects centrosome repositioning in T cells by controlling MT length, we turned to modelling. Our simulations predict that a relatively small number of KIF21B molecules is sufficient to restrict MT length. The attachment of a KIF21B molecule to the tip of a MT induces a MT pause. After this pause, the MT switches to shrinkage, and the KIF21B motor detaches. While the MT shrinks, the KIF21B molecule can bind to the next growing MT. Because of this dynamic process of binding to, inducing shrinkage of, and unbinding from MTs, 10 KIF21B motors can, in principle, induce shrinkage of 100 MTs within 100 seconds. In the model, we assumed that all KIF21B molecules induce a catastrophe, which differs from our experimental findings (Figure 3H). However, even if only half of the KIF21B molecules induce catastrophe, as in our experimental data, the total number of KIF21B molecules needed to significantly inhibit MT overelongation would still be relatively small, and this would also likely be true even in a three-dimensional system, where the diffusional space for the KIF21B molecules would be larger and the probability to bind to a MT lower. This length regulation by only a small number of KIF21B molecules could be validated experimentally by different labeling strategies or in a reconstituted system *in vitro*.

Furthermore, the simulations provided a possible mechanistic explanation for the impairment of centrosome polarization by MT overgrowth. In cells where the nucleus is located between the centrosome and the synapse, as would often be the case in T cells migrating towards a chemoattractant (Roig-Martinez et al., 2019), the centrosome needs to pass it along one side to move to the synapse. This movement would require a force only on one side and thus an asymmetric organization of MTs reaching the synapse from the different sides of the nucleus. Such asymmetries likely originate from fluctuations in the number of MTs contacting the

synapse from different sides that occur more readily when the number of MTs is low. The fluctuation-based mechanism of asymmetry generation could explain why some KIF21B knockout cells do polarize and some fail to do so within the observation period.

Although this mechanism for the impaired centrosome polarization in the absence of KIF21B appears plausible, its generalization could be limited by our model assumptions. To reduce complexity, we based our simulations on the force generation by dynein through MT sliding rather than through a MT end-on capture-shrinkage mechanism (Yi et al., 2013). Our model suggests that movement of the centrosome during polarization is a direct effect of a non-zero force along the MT network on one side of the nucleus. The mechanism of how this force is generated does not change the reliance on the force imbalance along the nucleus. It is possible that the precise trajectory of the centrosome depends on the molecular mechanism of how dynein generates the force (Hornak and Rieger, 2020). A comparison between experimentally determined centrosome trajectories and simulation results is beyond the scope of this study, and thus we cannot resolve the precise force generation mechanism of dynein. Our simulations suggest that when centrosome translocation is impaired, the MT network is experiencing balanced forces. As a consequence, we predict that in these situations one would observe major deformations of the nucleus, because it is trapped in a contracting cage of MTs spanning between the centrosome and the synapse. These deformations could also allow the centrosome to be located half-way between an apical and a basal position of the cell (Figure 4H). In our simulations, we assume a relatively stiff nucleus and therefore we only find the centrosome in an apical or basal position. It could be also possible that nuclear deformations push MTs towards the synapse, where they form dense peripheral MT bundles to accommodate the least curvature (Figure 2A and B).

A necessary assumption to set up a computable *Cytosim* simulation was the description of a T cell as a two-dimensional system. Because of this dimensionality reduction, it is not possible to quantitatively compare all experimental results to the results of our simulations. For example, the average MT length as experimentally determined in the 3D system exceeds by approximately twofold the average MT length determined in our 2D simulations. Constraining the average MT lengths from the experiments in our 2D simulations would lead to an overcrowded system that is difficult to solve computationally. Therefore, our approach to calibrate the model to the measured MT dynamics seems the most reasonable. It is possible that in a three-dimensional system, the locked centrosome state is more unstable than we conclude from our two-dimensional simulations, because the third dimension provides an additional

degree of freedom to break the force balance. However, a previous computational model in three dimensions suggested that in a T cell with a static overgrown MT network the centrosome can be trapped behind the nucleus (Kim and Maly, 2009), and in our ExM data we do observe KIF21B-KO cells with an apically located centrosome and symmetric MT bundles extending to the synapse from different sides (Figure 2 – figure supplement 1B). It is important to note that in other cells in our ExM samples the centrosome is located on the side of the nucleus, a situation that would lead to rapid polarization in our simulations. Since a significant proportion of cells shows a polarization delay in our experiments, it is unlikely that trapping of the centrosome behind the nucleus is the sole explanation of the polarization defect. It is possible that also in situations where the centrosome is positioned on the side of the nucleus, MT overgrowth leads to force balance and prevents efficient centrosome translocation. Furthermore, other mechanisms that are not included in the simulations likely contribute to the inhibition of centrosome repositioning by overgrown MTs. Excessively long MTs could slow down centrosome translocation by directly affecting dynein-mediated force generation, for example, by reducing the number of MT ends contacting the synapse and perturbing MT end capture by dynein. Long MTs could also make MT depolymerization-driven "reeling in" of the centrosome less efficient or create pushing forces and friction that would inhibit repositioning of the MT network. We further note that even in cells that did relocate their centrosome, the immunological synapses formed slower and were smaller, suggesting that the presence of circular MT bundles might perturb synapse formation in some additional ways, for example, by affecting signaling-based cross-talk between MTs and actin (Dogterom and Koenderink, 2019).

Taken together, our data show that the typical features of MT network organization in T cells, with relatively short and sparse MTs, is functionally important and that its maintenance depends on a dedicated regulatory factor, KIF21B, which restricts MT growth.

Methods

Cell culture, spreading assays and drug treatment

Jurkat T cells (clone E6.1; ATCC TIB-152) were grown in RPMI 1640 medium w/ L-Glutamine (Lonza) supplemented with 10% Fetal Bovine Serum and 1% penicillin/streptomycin. For all spreading assays, coverslips were coated with poly-D-lysine (Thermo Fisher Scientific, A3890401), washed with phosphate buffered saline (PBS) and incubated overnight at 4° C with a mouse monoclonal anti-CD3 antibody (clone UCHT1, StemCell Technologies, #60011) or a mouse monoclonal anti-HA antibody (clone 16B12, Biolegend (Covance), MMS-101P) at 10 µg/mL in PBS, except for the not-activated conditions, here cells were incubated on poly-D-lysine coated coverslips for 10 or 30 min prior to fixation. For live-cell imaging, Lab-Tek chambers (Thermo Fisher Scientific, 155409) were incubated overnight at 4° C with anti-CD3 (Clone UCHT1, StemCell Technologies, #60011) 10 µg/mL in PBS. Prior to spreading, cells were spun down for 4 min at 1000 rpm and resuspended in fresh pre-warmed RPMI 1640 medium.

Vinblastine (Sigma-Aldrich) treatment was performed by spinning down the cells for 4 min at 1000 rpm and resuspending the cells in pre-warmed medium containing 0.5 nM vinblastine 30 min prior to fixation. For live-cell imaging experiments, cells were resuspended in medium and 30 min prior to imaging, an equal amount of medium with 1 nM vinblastine was added to the cells to achieve a final concentration of 0.5 nM vinblastine.

Cell lines were routinely checked for mycoplasma contamination (LT07-518 Mycoalert assay, Lonza).

CRIPSR/Cas9 knockouts, lentivirus transduction and DNA constructs

KIF21B knock-out cell lines were generated in Jurkat cells (clone E6.1) using CRISPR/Cas9 technology. Jurkat T cells were transfected using an Amaxa Cell Line Nucleofector® kit V (Lonza), program X-005 with the pSpCas9(BB)-2A-Puro (PX459) vector (Addgene, #62988) bearing the appropriate targeting sequence (KIF21B: 5'-caccgTGTGTGAGCAAGCTCATCGA-3'). Cells were selected using 2 µg/mL puromycin (InvivoGen).

cDNA for lentivirus constructs were derived from the following sources: human cDNA clone KIAA 0449 for KIF21B (Kazusa DNA Research Institute), the EB3-GFP coding sequence as

described in (Stepanova et al., 2003), and the β-tubulin coding sequence was provided by Prof. Dr. Kai Jiang. KIF21B-GFP and β-tubulin-GFP sequences were cloned in pLVX-IRES-Puro vectors (Clontech), EB3-GFP was cloned in pLVX-IRES-Hygro vector (Clontech). EB3-mCherry construct (Stepanova et al., 2003) was transiently transfected using Amaxa Cell Line Nucleofector kit V (Lonza), program X-001.

Lentiviruses were produced by MaxPEI-based transfection of HEK293T (ATCC CRL-11268) cells with the construct of interest and the packaging vectors psPAX2 and pMD2.G (Addgene). Cell supernatant was harvested 48 and 72 hrs after transfection, filtered through a 0.45 µm filter and incubated overnight at 4° C in a polyethylene glycol (PEG) 6000-based precipitation buffer containing 80 g/L PEG 6000 and 82 mM NaCl at pH 7.2. The precipitation mix was centrifuged to concentrate the virus. The pellet containing the lentivirus was resuspended in PBS and Jurkat T cells were transduced in complete medium supplemented with 8 µg/mL polybrene (Merck-Millipore, TR-1003-G) using a spinoculation protocol: centrifugation of the transduction mix for 30 min at 2400 rpm at 32° C. Cells were selected using 2 µg/mL puromycin (InvivoGen, ant-pr5b) or with 100 µg/mL hygromycin (InvivoGen, ant-hm), five days after transduction.

Western blotting and antibodies

Jurkat T cells were lysed in a lysis buffer containing 20 mM Tris (pH 7.5), 150 mM NaCl, 1% Triton X-100 and cOmplete protease inhibitor cocktail (Roche, 4693132001). For Western blotting, we used the following polyclonal rabbit antibodies: anti-KIF21B (Sigma-Aldrich, HPA027249), anti-GFP (Abcam, ab290); and the following mouse monoclonal antibodies: anti-CD3 (Clone UCHT1, StemCell Technologies, #60011) and anti-Ku80 (BD Bioscience, 611360). The following secondary antibodies were used for Western blotting: IRDye-800CW-conjugated goat antibody against mouse IgG (#P/N 925-32210) and IRDye-680LT-conjugated goat antibody against rabbit IgG (#P/N 925-68021), both purchased from Li-Cor Biosciences.

For immunofluorescence staining, we used a rabbit polyclonal antibody against CEP135 (Sigma-Aldrich, SAB4503685). A rabbit monoclonal antibody against Lamtor4 (clone D6A4V, Cell Signaling Technology, #12284) and α-tubulin (clone EP1332Y, Abcam, ab52866). A mouse monoclonal antibody against α-tubulin (Sigma-Aldrich, T6199), and a rat monoclonal antibody against α-tubulin (clone γL1/2, Abcam, ab6160). The following secondary antibodies were used for immunofluorescence: Alexa-Fluor-488-conjugated goat antibodies against mouse and rabbit (#A27023 and #A-11034), Alexa-Fluor-594-conjugated goat antibodies

against mouse, rabbit and rat (#A-11032, #R37117 and #A-11007) and an Alexa-Fluor-647-conjugated antibody against mouse (#A-21240); all these antibodies were purchased from Life Technologies. F-actin was stained using Alexa-Fluor-488 or 594-conjugated phalloidin (Life Technologies, #12379, #12381).

T cell stimulation, RNA isolation and qRT-PCR analysis

T cells were stimulated with a combination of Phorbol 12-myristate 13-acetate (PMA) (Sigma-Aldrich, P8139) and ionomycin (Sigma-Aldrich, I0634) at indicated time points and concentrations. Cells were collected on ice and total RNA was extracted using TRIzol reagent (Thermo Fisher Scientific, 15596026) and cDNA synthesis was performed using the iScript cDNA synthesis kit (Bio-Rad, 1708891). cDNA samples were amplified with SYBR Select mastermix (Life Technologies, 44-729-19) using a QuantStudio 12K Flex Real-Time PCR System (Applied Biosystems) and the following RT-PCR primer pairs: IL-2 forward 5'-AACTCACCAGGATGCTCACATTTA-3', IL-2 reverse 5'-TCCCTGGGTCTTAAGTGAAAGTTT-3' and GAPDH forward 5'-CAACGGATTTGGTCGTATT-3' and GAPDH reverse 5'- GATGGCAACAATATCCACTT-3'. The LIVAK method was used to calculate relative mRNA expression in respect to the housekeeping gene GAPDH.

Immunofluorescence staining and image acquisition

For immunofluorescence staining of tubulin and CEP135 for TIRF microscopy, cells were fixed in −20°C methanol for 10 min, followed by washes with PBS and permeabilization with PBS supplemented with 0.15% Triton X-100 for 2 min. All subsequent wash steps were performed using PBS supplemented with 0.05% Tween-20. Epitope blocking and antibody labeling steps were performed in PBS supplemented with 0.05% Tween-20 and 1% Bovine Serum Albumin (BSA). Before mounting in DAPI-containing Vectashield mounting medium (Vector Laboratories, H-1200-10), slides were washed with 70% and 100% ethanol and air-dried.

For immunofluorescence staining of lysosomes (Lamtor4) and centrosomes (CEP135) for 3D analysis, or labelling with Phalloidin, cells were fixed with 4% paraformaldehyde (PFA) in PBS at room temperature (RT) for 10 min, followed by washes with PBS and permeabilization with PBS supplemented with 0.15% Triton X-100 for 2 min. All subsequent wash steps were

performed using PBS supplemented with 0.05% Tween-20. Epitope blocking and antibody labeling steps were performed in PBS supplemented with 0.05% Tween-20 and 1% BSA. Samples were mounted using DAPI-containing Vectashield mounting medium (Vector Laboratories, H1200-10).

Widefield imaging on fixed cells was performed on a Nikon Eclipse Ni-E upright fluorescence microscope equipped with Plan Apo Lambda 100x N.A. 1.45 oil and 60x N.A. 1.40 oil objectives microscopes, ET-BFP2 (49021, Chroma), ET-GFP (49002, Chroma), ET-mCherry (49008, Chroma), ET-Cy5 (49006, Chroma) filter sets and a Photometrics CoolSNAP HQ2 CCD (Roper Scientific, Trenton, NJ) camera. The microscope was controlled by Nikon NIS Br software.

TIRF imaging on fixed cells was performed on an ILAS-2 system (Roper Scientific, Evry, France) with a dual laser illuminator for azimuthal spinning TIRF (or Hilo) illumination and with a custom modification for targeted photomanipulation. This system was installed on Nikon Ti microscope (with the perfect focus system, Nikon), equipped with 405 nm 100 mW Stradus (Voltran), 488 nm 150 mW Stradus (Voltran), 561 nm 100 mW Coherent (OBIS 561-100LS) and 642 nm 110 mW Stradus (Vortran) lasers; and ET-BFP (49021, Chroma), ET-GFP (49002, Chroma) and ET-mCherry (49008, Chroma) filter sets. Fluorescence signal was detected using an EMCCD Evolve mono FW DELTA 512x512 camera (Roper Scientific) with the intermediate lens 2.5X (Nikon C mount adapter 2.5X) or a CCD CoolSNAP MYO M-USB-14-AC camera (Roper Scientific). The final resolution using EMCCD camera was 0.065 µm/pixel, using CCD camera it was 0.045 µm/pixel. The setup was controlled with MetaMorph 7.8.8 software (Molecular Device).

Spinning disk microscopy was performed on inverted research microscope Nikon Eclipse Ti-E (Nikon), equipped with the perfect focus system (Nikon), Plan Apo VC 100x N.A. 1.40 oil objective (Nikon), spinning disk Yokogawa CSU-X1-A1 with 405-491-561-642 quad-band mirror (Yokogawa). The system was also equipped with ASI motorized stage with the piezo plate MS-2000-XYZ (ASI), Back-Illuminated Evolve 512 EMCCD camera (Photometrics) or Back-Illuminated Prime BSI sCMOS camera (Photometrics) and controlled by the MetaMorph 7.10 software (Molecular Devices). 405 nm 100 mW Stradus (Voltran), 491 nm 100 mW Calypso (Cobolt), 561 nm 100 mW Jive (Cobolt) and 642 nm 110 mW Stradus (Vortran) lasers were used as the light sources. The setting was equipped with ET-BFP2 (49021, Chroma), ET-GFP (49002, Chroma), ET-mCherry (49008, Chroma) and ET-Cy5 (49006, Chroma) filter sets to image blue, green, red and far-red fluorescence signals, respectively. 16-bit images were

projected onto the Evolve 512 EMCCD camera with intermediate lens 2.0X (Edmund Optics) at a magnification of 0.066 µm/pixel or onto Prime BSI sCMOS camera with no intermediate lens at a magnification of 0.063 µm/pixel. Z-stacks of cells were acquired with a step size of 0.1 µm.

Immunofluorescence staining and image acquisition for STED microscopy and ExM

For all STED and ExM samples, 1.5 mm thick coverslips (Marienfeld, 0107032) were used. Jurkat cells were added to anti-CD3 coated coverslips for indicated time points. Cells were pre-extracted for 1 min with pre-warmed (37°C) extraction buffer composed of MRB80 (80 mM K-PIPES pH 6.8, 4 mM $MgCl_2$, 1mM EGTA) supplemented with 0.35% Triton X-100 and 0.2% glutaraldehyde. After extraction, cells were fixed for 15 min with pre-warmed (37°C) 4% PFA in PBS. All subsequent wash steps were performed using PBS supplemented with 0.2% Triton X-100. Epitope blocking and antibody labeling steps were performed in PBS supplemented with 3% BSA. Labelling with primary antibodies was performed overnight at 4°C. After washing with PBS, labelling with secondary antibodies was performed for 3 hrs at RT. For STED microscopy samples, cells were washed with PBS and MiliQ and air dried. Cells were mounted in Prolong Gold (Thermo Fisher).

For ExM, we followed the procedures described by (Jurriens et al., 2020). Samples were post-fixed with 0.1 mg/mL acryloyl X-SE (AcX) (Thermo Fisher, A20770) in PBS overnight at RT. For gelation, monomer solution was prepared containing 2M NaCl, 8.625% sodium acrylate (Sigma-Aldrich, 408220), 2.5% acrylamide (AA), 0.15% N,N'-methylenebisacrylamide (BIS) in PBS. As a source of AA we used 37.5:1 AA/BIS solution (Sigma-Aldrich, A3699) and supplemented it with BIS (Sigma-Aldrich, M1533) to reach final concentrations. Gelation of the monomer solution was initiated with 0.2% ammonium persulfate (APS) and 0.2% tetramethylethylenediamine (TEMED) and 170 uL was transferred to a silicone mold with inner diameter of 13 mm (Sigma-Aldrich, GBL664107) attached to a parafilm-covered glass slide, with the sample put cell-down on top to close off the gelation chamber. After incubation at RT for 1-3 min, the sample was transferred to a humidified 37°C incubator for at least 30 min to fully polymerize the gel. After gelation, the gel was transferred to a 12-well plate and digested in TAE buffer (containing 40 mM Tris, 20 mM acetic acid and 1 mM EDTA) supplemented with 0.5% Triton X-100, 0.8 M guanidine-HCl and 7.5 U/mL Proteinase-K (Thermo Fisher, EO0491) for 4 hrs at 37°C. The gel was transferred to a Petri dish, water was exchanged twice

after 30 min and sample was left in water to expand overnight in 50 mL MiliQ. Prior to imaging the cells were trimmed and mounted.

All STED and ExM images have been acquired using a Leica TCS SP8 STED 3X microscope equipped with a HC PL Apo 100x/1.40 Oil STED WHITE objective for STED acquisition and a HC PL APO 86x/1.20W motCORR STED (Leica 15506333) water objective for ExM. A pulsed white laser (80 MHz) was used for excitation, and when using STED a 775 nm pulsed depletion laser was used. The internal Leica GaAsP HyD hybrid detectors were used with a time gate of $1 \leq tg \leq 6$ ns. The set-up was controlled using LAS X. If required, drift correction was performed on ExM acquisitions using Huygens Software (Scientific Volume Imaging).

Live-cell imaging

Live-cell DIC imaging was performed on an inverted Nikon Ti microscope equipped a perfect focus system (Nikon), a Plan Fluor 40x/1.30 Oil DIC objective, a CoolSNAP HQ2 CCD camera (Photometrics), a motorized stage MS-2000-XYZ with Piezo Top Plate (ASI), and a stage top incubator (TokaiHit) set to 37° C. The microscope was controlled by MicroManager software.

Jurkat cells were live imaged on an ILAS-2 system (Roper Scientific, Evry, France) is a dual laser illuminator for azimuthal spinning TIRF (or Hilo) illumination and with a custom modification for targeted photomanipulation. This system was installed on Nikon Ti microscope (with the perfect focus system, Nikon), equipped with a Nikon Apo TIRF 100x N.A. 1.49 oil objective (Nikon); 488 nm 150 mW Stradus (Voltran) and 561 nm 100 mW Coherent (OBIS 561-100LS) lasers; and ET-GFP (49002, Chroma) and ET-mCherry (49008, Chroma) filter sets. For simultaneous imaging of green and red fluorescence, we used an ET-GFP/mCherry filter cube (59022, Chroma) together with an Optosplit III beamsplitter (Cairn Research Ltd) equipped with double-emission filter cube configured with ET525/50m, ET9630/75m and T585lprx (Chroma). Fluorescence signal was detected using an EMCCD Evolve mono FW DELTA 512x512 camera (Roper Scientific) with the intermediate lens 2.5X (Nikon C mount adapter 2.5X) or a CCD CoolSNAP MYO M-USB-14-AC camera (Roper Scientific) The setup was controlled with MetaMorph 7.8.8 software (Molecular Device). To keep cells at 37° C, a stage top incubator model INUBG2E-ZILCS (Tokai Hit) was used. Or on an inverted research microscope Nikon Eclipse Ti-E (Nikon) with the perfect focus system (PFS) (Nikon), equipped with Nikon CFI Apo TIRF 100 × 1.49 N.A. oil objective (Nikon). For excitation lasers we used 491 nm 100 mW Stradus (Vortran). We used an ET-GFP 49002 filter

set (Chroma) for imaging of proteins tagged with GFP. Fluorescence signal was detected using an an Evolve512 EMCCD camera (Photometrics) or a CoolSNAP HQ2 CCD camera(Photometrics). The setup was controlled with MetaMorph 7.8.8 software (Molecular Device). To keep cells at 37° C, a stage top incubator model INUBG2E-ZILCS (Tokai Hit) was used.

Image processing and analysis

Images and movies were processed using ImageJ. All images were modified by linear adjustments of brightness and contrast. Average intensity projections and z-projections were made using the z projection tool. Kymographs were made using the ImageJ plugin KymoResliceWide v.0.4 (https://github.com/ekatrukha/KymoResliceWide; copy archived at https://github.com/elifesciences-publications/KymoResliceWide).

Cell surface area

Cell surface area was measured manually by drawing the cell circumference using the freehand tool in ImageJ. For KIF21B-GFP overexpressing rescue cell lines, very low expressing or GFP-negative cells were not measured.

Cell volumes

Cell volumes were measured based on Phalloidin staining of 3D-imaged Jurkat cells imaged on a Spinning disk confocal microscope. Imaris software (Bitplane/Oxford instruments, version 9.5.1) was used to manually create a cell surface mask using the Isosurface Drawing mode set at 10% density. The cell outline was determined for > 10 positions in z-dimension to create a 3D volume rendering of the Jurkat cell from which the volume was determined using the Statistics feature of the Imaris software.

MT organizing (TIRF microscopy)

For quantifying MT organization in T cells in different KIF21B-KO and rescue conditions, we classified MT networks as “radial” when a clear aster-like MT pattern was observed with an obvious presence of a microtubule organizing center or CEP135-positive fluorescent signal in the TIRF field. Other MT networks were classified as “disorganized” when an aster-like organization indicative of a polarized centrosome was lacking.

3D analysis of lysosomes and centrosomes

To quantify polarization of lysosome clusters in T cells, the distance of these Lamtor4-positive clusters and the anti-CD3-positive coverslip was measured in z. A reslice was made of the entire cell to have a z-projection from which an average intensity projection was made to create a landscape of fluorescence intensities in z. The distance between coverslip and lysosome cluster was determined by taking the distance between the coverslip and the pixel row in z that contained the peak intensity value of all rows. A Lamtor4-stained lysosome cluster was quantified as "polarized" when its peak intensity value was localized within 2 µm distance from the anti-CD3-stained coverslip.

For centrosome polarization quantifications, the distance between the CEP135-stained centrosome and the anti-CD3-positive coverslip was measured in z. A line scan was drawn over the centrosome and a reslice was made to make a z-projection of the cell at the location of the centrosome. The distance between coverslip and centrosome was determined by drawing a line from the center to center of both fluorescence signals. A CEP135-stained centrosome was quantified as "polarized" when it was localized within 2 µm distance from the anti-CD3-stained coverslip.

STED microscopy

STED images of fluorescently labeled MTs were analyzed using ImageJ. Images were background subtracted using the Background Subtraction tool with a rolling ball radius of 50 pixels and were separated into radial and non-radial components using a customized ImageJ macro (*https://github.com/ekatrukha/radialitymap*)(Martin et al., 2018). In short, we used the 'Cubic Spline Gradient' method and Tensor Sigma parameter of 8 pixels to calculate a radial and a non-radial map image that illustrate the separated radial and non-radial components of the original picture. For both the original image and images showing the separated components, radial intensity profiles were made from the centrosome to the farthest removed portion of the cell periphery using the Radial Profile Angle plugin at a 45 degree integration angle. To quantify the non-radiality of the MT organisation per cell, the areas under the curve (AUC) of the radial intensity profiles of the original image (total intensity) and of the non-radial map images were calculated using Excel. The non-radial intensity as percentage of the total intensity was calculated using: $(AUC_{non\text{-}radial}/AUC_{Total\ intensity})*100$.

ExM microscopy

For the ExM analyses and all 3D renders Imaris (Bitplane/Oxford instruments, version 9.5.1) was used. Using the Automatic Spot Detection algorithm (set to 10 µm), the centrosome was localized in the 3D renderings as the brightest spot present; and a sphere was generated around the centrosome with a radius of 5 µm. A second sphere was generated with a radius of 6 µm using the Automatic Spot Detection (set to 11 µm). From these two spheres, a spherical shell was generated with an inner spacing thickness of 1 µm using the following steps: all voxels outside the surface of the smaller sphere and all voxels inside the surface of the bigger sphere were set to the maximum intensity value (255). Using the Colocalization function a colocalization channel of both masks was made which generated the spherical shell used for all further quantifications.

To analyze MTs within this spherical shell, a colocalization channel was generated for the tubulin channel using the Colocalization function. Thresholds were adjusted to include all MTs. Based on this colocalization channel, surface masks were generated for the tubulin signal using the Surfaces tool with Split Touching Objects enabled (seed points diameter set at 0.45µm). Seed points and generated surfaces were visually filtered so that all MTs were included. To count the number of MTs, all generated surfaces were checked and the number of MTs were counted manually per spherical shell. The mean intensity corresponding to 1 µm MT was determined from the fluorescence intensity per surface (using the Statistics feature of the Imaris software) corrected for the manually counted number of MTs in each surface. To determine the total fluorescence intensity corresponding to the complete MT network the Surfaces tool was used to generate a surface mask covering the entire MT network (Split Touching Objects setting disabled) and used an automatic threshold to discard very small nonspecific surfaces. To estimate the average MT length, the total intensity as found (using the Statistics feature of the Imaris software) was divided by the MT intensity per micron and by the number of MTs.

Quantification of live-cell imaging

The duration of synapse formation imaged using DIC microscopy was quantified using kymographs. Kymographs were generated using the ImageJ plugin KymoResliceWide v.0.4. along a line from the center of the cell to the cell periphery showing least irregular cell

spreading. Cells that exhibited drift on the coverslip during spreading were not used for quantification. The initiation of synapse formation was determined as the moment where the cell started to spread sideways. The synapse was at maximum size when sideway spreading became static (velocity < 0.5 µm/min). The duration of synapse formation was determined as the duration at which the Jurkat cell exhibited sideward spreading at a minimum mean velocity of 1 µm/min.

EB3-GFP growth rates were quantified using kymographs that were generated using the ImageJ plugin KymoResliceWide v.0.4. The slope of EB3-GFP growth events in these kymographs were used to calculate growth rates corrected for acquisition settings. Catastrophe rates were quantified by determining the inverse value of growth time of EB3-GFP growth events.

Single molecule KIF21B velocities were quantified from TIRF-imaged KIF21B-GFP expressing T cells using kymographs that were generated using the ImageJ plugin KymoResliceWide v.0.4. The slope of motile KIF21B-GFP events in these kymographs were used to calculate kinesin velocities corrected for acquisition settings. These values were fitted to a Gaussian curve to determine mean KIF21B velocity.

Single kinesin events at MT plus ends were quantified using TIRF-imaged KIF21B-GFP expressing T cells that were transfected with EB3-mCherry as a marker of growing MT plus ends. Events were quantified when a motile KIF21B-GFP molecule (> 0.1 µm/s velocity) reached the end of a growing EB3-mCherry-positive MT. KIF21B-GFP behavior after a MT plus-end encounter was categorized as “pausing”, “tip-tracking” or “dissociation”. The “tip-tracking” events, where KIF21B tracked a growing plus end at the same velocity as EB3 signal, were subsequently sub-categorized into “tip-tracking + pausing” and “tip-tracking + dissociation” events. The state of the EB3-mCherry-positive plus end was defined as “growing” (> 0.05 µm/s growth velocity) or “static” (< 0.05 µm/s growth velocity) for KIF21B-GFP events that went into a paused state, regardless whether there was tip-tracking or not. The fate of EB3-mCherry plus ends after encountering a pausing KIF21B-GFP molecule was divided into four categories: “pausing + catastrophe”, “pausing + growth re-initiation”, “growth continuation without pausing” or “not determined” for the events that were unclear or took place beyond acquisition time. The fate of EB3-mCherry plus ends after encountering a KIF21B-GFP molecule that directly dissociated upon reaching the plus end was divided into three categories: “no effect”, “coincided with MT pausing” or “coincided with MT catastrophe”. Pause times were quantified for KIF21B-GFP molecules that that appeared static (< 0.1 µm/s velocity and ≥ 0.5 s duration) and underwent pausing at an EB3-mCherry-positive MT plus end. Pause times

were quantified for growing EB3-mCherry MT plus ends that appeared static (< 0.05 µm/s growth velocity and ≥ 0.5 s duration) and transitioned into a paused state after an encounter with a KIF21B-GFP molecule. The end time of a pause coincided with either a catastrophe or a growth re-initiation event.

For analysis of β-tubulin-GFP imaging, we scored the fate of growing MTs reaching the plasma membrane into four categories: catastrophe, sliding along the cortex, MT buckling and pausing. Quantified events had to meet the following criteria: 1) events at the MT plus end had to be preceded by a phase of growth before reaching the plasma membrane; 2) the acquisition time had to include a complete pausing event or, in the case of a catastrophe, sliding or buckling event, the initiation of the event. Pause events and pause times were quantified for MT plus ends that appeared static (< 0.05 µm/s growth velocity and ≥ 0.5 s duration). For determining pause duration of a MT reaching the plasma membrane, a kymograph was generated for the growing MT using the ImageJ plugin KymoResliceWide v.0.4 and the length of the pause was determined by the number of vertical pixels in the kymograph multiplied by the exposure time.

Single molecule intensity analysis

Single-molecule fluorescence histograms of monomeric GFP (control) or kinesins moving on MTs intracellularly were built from acquisitions made on a TIRF microscope. To ensure identical imaging conditions, a single imaging slide (with a plasma cleaned coverslip) was used containing two flow chambers to image GFP (control) and KIF21B-GFP expressing T cells. For purified GFP, we used cell lysates from HEK293T cells overexpressing monomeric GFP. The GFP protein was diluted in PBS and added to an imaging flow chamber; chambers were subsequently washed with PBS, leaving a fraction of the GFP proteins immobilized on the coverslip. Protein dilution was optimized to provide images of ~0.05 fluorophores/µm2 for GFP control conditions. For T cells expressing KIF21B-GFP, the imaging chamber was incubated overnight at 4° C with 10 µg/mL of a mouse monoclonal anti-CD3 (clone UCHT1, StemCell Technologies, #60011) in PBS. The chamber was washed three times with PBS and one time with RPMI 1640 medium. T cells expressing KIF21B-GFP were concentrated in RPMI 1640 medium and added to the chamber 2 min before imaging. After sealing the chambers with vacuum grease to prevent evaporation, samples were imaged on a TIRF microscope at 37° C. For monomeric GFP, ~40 images were acquired at 100 ms exposure time at different positions on the coverslip to avoid pre-bleaching. For moving kinesins, ~5–10 cells

were imaged using stream acquisition at a 100 ms exposure time per frame. All acquisitions were obtained under identical laser power and a TIRF angle with a calibrated penetration depth *d* of 180 nm.

ImageJ plugin DoM_Utrecht v.1.1.6 was used to for detection and fitting of single molecule fluorescent spots as described previously (Yau et al., 2014). In short, individual spots were fitted with 2D Gaussian and the amplitude of the fitted Gaussian function was used as a measure of the fluorescence intensity value of an individual spot. For moving KIF21B-GFP molecules in T cells, ImageJ plugin DoM_Utrecht v.1.1.9 was used for detection and fitting of single molecule fluorescent spots. Using this plugin, these particles were linked to tracks with a maximum distance to search over one frame of 3 pixels and a maximum linking gap of 2 pixels. Tracks were filtered for a duration of ≥ 1 s. The histograms were fitted to lognormal distributions using GraphPad Prism 8. A correction factor (c) was calculated for KIF21B-GFP fitted peak intensities (i) for a series (0-100 nm) of hypothetical distances (h) between the coverslip and KIF21B molecule using the formula:

$$\boldsymbol{c} = \frac{\boldsymbol{i}}{\boldsymbol{e}^{-\left(\frac{\boldsymbol{h}}{\mathbf{180}}\right)}}$$

Cytosim modeling

The T cell model was made in the agent-based modeling structure *Cytosim* (Nedelec and Foethke, 2007), which solves overdamped Langevin equations to calculate the movement of the cytoskeleton and associated proteins. We choose *Cytosim* to be able to explicitly model the dynamics of KIF21B and dynein and to ensure an easy reproducibility of our results. *Cytosim* is open-source and together with our configuration file easy to run. For generating plots and figures, we used Python with Seaborn, NumPy and Pandas libraries.

To set up a simulation of the MT network and the associated proteins of a T cell we used the following features and elements.

Shape

The shape of the T cell is encoded as SpaceHemisphere. This space definition makes a circular (2D) or spherical (3D) space, where a plane intersects the space at arbitrary height. In the T cell, this is at 0.9 of the full height. In the space we use to confine the centrosome during

initialization this is at 0.2 of the full height of the cell. The corners of the plane are curved, to avoid infinitesimal corners. The curved corners are calculated by finding a smaller circle that interpolates continuously between the synapse and the (circular) cell shape. Any interaction with the shape is calculated by finding the closest point on the space surface and applying a linear force in this direction. If objects are outside of the space, they are pushed inwards.

Steric Interactions

Because we simplified our T cell to a two-dimensional object, we needed to adjust the steric interactions. Fibers in the simulations cannot enter the nucleus, but can cross one another to effectively mimic the third dimension. This behavior is achieved by the ‘ad-hoc’ steric interactions within *Cytosim*, in which we compare the position of each fiber segment with the nucleus, and if the fiber segment is within the nucleus, a linear force is applied to push the fiber out, similar to cell shape confinement.

Dynein

Dynein motors are uniformly distributed and anchored at the synapse. They bind to MT in their vicinity and walk along them. The walking speed is characterized by a linear force-velocity relation as typically modeled in *Cytosim*. This definition describes a cortically anchored dynein that slides MTs, which is different from the end-on capture mechanism proposed by (Yi et al. 2013).

KIF21B

The KIF21B units are modeled as a new form of binding Hand in *Cytosim*: the Capper hand. They are able to bind and walk on the fiber. When they reach a fiber’s tip, the fiber is set to a paused state, neither growing or shrinking. The waiting time for the motor at a fiber’s tip is redrawn from a distribution to ensure that the pause length is correctly implemented, regardless of how long the Capper has already walked on the fiber. If a Capper unbinds, it sets the MT to the shrinkage state. Subsequently, any other bound Cappers unbind.

As KIF21B is localized in the cytosol, we extended the ad-hoc steric interactions to Singles. Because Singles are modeled as molecules with a negligible inertia displaying a random walk, we cannot easily apply elastic forces to these objects. Thus, we model the KIF21B units to bounce off the nucleus, similar to its interaction with the shape. If a good bounce location cannot be found after 1000 attempts (i.e. the molecule is in a tight corner between nucleus and cell shape), the molecule is set to the edge of the nucleus.

Fitting KIF21B-KO MT dynamics

To match the parameterization of our model to the MT dynamics in the KIF21B-KO system we used a separate *Cytosim* simulation to mimic the experimental data from the TIRF imaging of the MT dynamics at the synapse. Ultimately this approach suggested a linear relation between the free growing catastrophe rate and the growing force, which is the characteristic force of the MT polymerization. This relation fulfills the constraint that 81% of the MT in the TIRF data did not initiate catastrophe within 3.3 s, while satisfying the 0.3 s^{-1} stalled catastrophe rate. More details are included in Figure 5 – figure supplement 1A-D.

In all simulations outside of fitting the KIF21B-KO MT dynamics, MTs are initialized with slightly different lengths, pulled from an exponential distribution with the mean of 1 µm. This was done so that even with very small catastrophe rates, MT lengths would not be equal. Simulations were run in a slightly altered version of *Cytosim* to be able to immobilize the centrosome in the center of the synapse (http://doi.org/10.5281/zenodo.4312942).

Data and software availability

The data supporting the conclusions are included in the manuscript. The numerical data shown in all plots are included as "source data"; uncropped Western blots are included as a figure supplement (Figure 1 – figure supplement 1). The code of our simulations is hosted on http://doi.org/10.5281/zenodo.4312942.

Acknowledgements

This work was supported by the European Research Council Synergy grant 609822 and Netherlands Organization for Scientific Research ALW Open Program grant 824.15.017 to A.A, as well as the European Research Council Consolidator Grant 819219 to L.C.K.

Competing financial interests

The authors declare no competing financial interests.

References

Aher, A., Kok, M., Sharma, A., Rai, A., Olieric, N., Rodriguez-Garcia, R., Katrukha, E.A., Weinert, T., Olieric, V., Kapitein, L.C*., et al.* (2018). CLASP Suppresses Microtubule Catastrophes through a Single TOG Domain. Dev Cell *46*, 40-58.

Anderson, C.A., Massey, D.C., Barrett, J.C., Prescott, N.J., Tremelling, M., Fisher, S.A., Gwilliam, R., Jacob, J., Nimmo, E.R., Drummond, H*., et al.* (2009). Investigation of Crohn's disease risk loci in ulcerative colitis further defines their molecular relationship. Gastroenterology *136*, 523-529.

Andres-Delgado, L., Anton, O.M., Bartolini, F., Ruiz-Saenz, A., Correas, I., Gundersen, G.G., and Alonso, M.A. (2012). INF2 promotes the formation of detyrosinated microtubules necessary for centrosome reorientation in T cells. J Cell Biol *198*, 1025-1037.

Asselin, L., Rivera Alvarez, J., Heide, S., Bonnet, C.S., Tilly, P., Vitet, H., Weber, C., Bacino, C.A., Baranano, K., Chassevent, A*., et al.* (2020). Mutations in the KIF21B kinesin gene cause neurodevelopmental disorders through imbalanced canonical motor activity. Nat Commun *11*, 2441.

Barrett, J.C., Hansoul, S., Nicolae, D.L., Cho, J.H., Duerr, R.H., Rioux, J.D., Brant, S.R., Silverberg, M.S., Taylor, K.D., Barmada, M.M*., et al.* (2008). Genome-wide association defines more than 30 distinct susceptibility loci for Crohn's disease. Nat Genet *40*, 955-962.

Belyy, V., Schlager, M.A., Foster, H., Reimer, A.E., Carter, A.P., and Yildiz, A. (2016). The mammalian dynein-dynactin complex is a strong opponent to kinesin in a tug-of-war competition. Nat Cell Biol *18*, 1018-1024.

Bianchi, S., van Riel, W.E., Kraatz, S.H., Olieric, N., Frey, D., Katrukha, E.A., Jaussi, R., Missimer, J., Grigoriev, I., Olieric, V*., et al.* (2016). Structural basis for misregulation of kinesin KIF21A autoinhibition by CFEOM1 disease mutations. Sci Rep *6*, 30668.

Bieling, P., Telley, I.A., and Surrey, T. (2010). A minimal midzone protein module controls formation and length of antiparallel microtubule overlaps. Cell *142*, 420-432.

Bouchet, B.P., Noordstra, I., van Amersfoort, M., Katrukha, E.A., Ammon, Y.C., Ter Hoeve, N.D., Hodgson, L., Dogterom, M., Derksen, P.W.B., and Akhmanova, A. (2016). Mesenchymal Cell Invasion Requires Cooperative Regulation of Persistent Microtubule Growth by SLAIN2 and CLASP1. Dev Cell *39*, 708-723.

Bringmann, H., Skiniotis, G., Spilker, A., Kandels-Lewis, S., Vernos, I., and Surrey, T. (2004). A kinesin-like motor inhibits microtubule dynamic instability. Science *303*, 1519-1522.

Bunnell, S.C., Kapoor, V., Trible, R.P., Zhang, W., and Samelson, L.E. (2001). Dynamic actin polymerization drives T cell receptor-induced spreading: a role for the signal transduction adaptor LAT. Immunity *14*, 315-329.

Bustos-Moran, E., Blas-Rus, N., Martin-Cofreces, N.B., and Sanchez-Madrid, F. (2017). Microtubule-associated protein-4 controls nanovesicle dynamics and T cell activation. J Cell Sci *130*, 1217-1223.

Chen, F., Tillberg, P.W., and Boyden, E.S. (2015). Optical imaging. Expansion microscopy. Science *347*, 543-548.

Cheng, L., Desai, J., Miranda, C.J., Duncan, J.S., Qiu, W., Nugent, A.A., Kolpak, A.L., Wu, C.C., Drokhlyansky, E., Delisle, M.M*., et al.* (2014). Human CFEOM1 mutations attenuate KIF21A autoinhibition and cause oculomotor axon stalling. Neuron *82*, 334-349.

Combs, J., Kim, S.J., Tan, S., Ligon, L.A., Holzbaur, E.L., Kuhn, J., and Poenie, M. (2006). Recruitment of dynein to the Jurkat immunological synapse. Proc Natl Acad Sci U S A *103*, 14883-14888.

Daza, R., Gonzalez-Bermudez, B., Cruces, J., De la Fuente, M., Plaza, G.R., Arroyo-Hernandez, M., Elices, M., Perez-Rigueiro, J., and Guinea, G.V. (2019). Comparison of cell mechanical measurements provided

by Atomic Force Microscopy (AFM) and Micropipette Aspiration (MPA). J Mech Behav Biomed Mater *95*, 103-115.

Dogterom, M., and Koenderink, G.H. (2019). Actin-microtubule crosstalk in cell biology. Nat Rev Mol Cell Biol *20*, 38-54.

Dogterom, M., and Yurke, B. (1997). Measurement of the force-velocity relation for growing microtubules. Science *278*, 856-860.

Doodhi, H., Prota, A.E., Rodriguez-Garcia, R., Xiao, H., Custar, D.W., Bargsten, K., Katrukha, E.A., Hilbert, M., Hua, S., Jiang, K.*, et al.* (2016). Termination of Protofilament Elongation by Eribulin Induces Lattice Defects that Promote Microtubule Catastrophes. Curr Biol *26*, 1713-1721.

Dustin, M.L., Chakraborty, A.K., and Shaw, A.S. (2010). Understanding the structure and function of the immunological synapse. Cold Spring Harb Perspect Biol *2*, a002311.

Filbert, E.L., Le Borgne, M., Lin, J., Heuser, J.E., and Shaw, A.S. (2012). Stathmin regulates microtubule dynamics and microtubule organizing center polarization in activated T cells. J Immunol *188*, 5421-5427.

Garcia-Etxebarria, K., Jauregi-Miguel, A., Romero-Garmendia, I., Plaza-Izurieta, L., Legarda, M., Irastorza, I., and Bilbao, J.R. (2016). Ancestry-based stratified analysis of Immunochip data identifies novel associations with celiac disease. Eur J Hum Genet *24*, 1831-1834.

Geiger, B., Rosen, D., and Berke, G. (1982). Spatial relationships of microtubule-organizing centers and the contact area of cytotoxic T lymphocytes and target cells. J Cell Biol *95*, 137-143.

Ghiretti, A.E., Thies, E., Tokito, M.K., Lin, T., Ostap, E.M., Kneussel, M., and Holzbaur, E.L.F. (2016). Activity-Dependent Regulation of Distinct Transport and Cytoskeletal Remodeling Functions of the Dendritic Kinesin KIF21B. Neuron *92*, 857-872.

Gittes, F., Mickey, B., Nettleton, J., and Howard, J. (1993). Flexural rigidity of microtubules and actin filaments measured from thermal fluctuations in shape. J Cell Biol *120*, 923-934.

Goris, A., Boonen, S., D'Hooghe M, B., and Dubois, B. (2010). Replication of KIF21B as a susceptibility locus for multiple sclerosis. J Med Genet *47*, 775-776.

Gromova, K.V., Muhia, M., Rothammer, N., Gee, C.E., Thies, E., Schaefer, I., Kress, S., Kilimann, M.W., Shevchuk, O., Oertner, T.G.*, et al.* (2018). Neurobeachin and the Kinesin KIF21B Are Critical for Endocytic Recycling of NMDA Receptors and Regulate Social Behavior. Cell Rep *23*, 2705-2717.

Guo, Q., Liao, S., Zhu, Z., Li, Y., Li, F., and Xu, C. (2018). Structural basis for the recognition of kinesin family member 21A (KIF21A) by the ankyrin domains of KANK1 and KANK2 proteins. J Biol Chem *293*, 557-566.

Gupta, M.L., Jr., Carvalho, P., Roof, D.M., and Pellman, D. (2006). Plus end-specific depolymerase activity of Kip3, a kinesin-8 protein, explains its role in positioning the yeast mitotic spindle. Nat Cell Biol *8*, 913-923.

He, M., Subramanian, R., Bangs, F., Omelchenko, T., Liem, K.F., Jr., Kapoor, T.M., and Anderson, K.V. (2014). The kinesin-4 protein Kif7 regulates mammalian Hedgehog signalling by organizing the cilium tip compartment. Nat Cell Biol *16*, 663-672.

Hooikaas, P.J., Martin, M., Muhlethaler, T., Kuijntjes, G.J., Peeters, C.A.E., Katrukha, E.A., Ferrari, L., Stucchi, R., Verhagen, D.G.F., van Riel, W.E.*, et al.* (2019). MAP7 family proteins regulate kinesin-1 recruitment and activation. J Cell Biol *218*, 1298-1318.

Hornak, I., and Rieger, H. (2020). Stochastic Model of T Cell Repolarization during Target Elimination I. Biophys J *118*, 1733-1748.

Howard, J., and Garzon-Coral, C. (2017). Physical Limits on the Precision of Mitotic Spindle Positioning by Microtubule Pushing forces: Mechanics of mitotic spindle positioning. Bioessays *39*, 10.1002/bies.201700122.

International Multiple Sclerosis Genetics, C. (2010). Comprehensive follow-up of the first genome-wide association study of multiple sclerosis identifies KIF21B and TMEM39A as susceptibility loci. Hum Mol Genet *19*, 953-962.

Janson, M.E., de Dood, M.E., and Dogterom, M. (2003). Dynamic instability of microtubules is regulated by force. J Cell Biol *161*, 1029-1034.

Jurriens, D., van Batenburg, V., Katrukha, E.A., and Kapitein, L.C. (2020). Mapping the neuronal cytoskeleton using expansion microscopy. In Methods in Cell Biology (Academic Press).

Kannan, M., Bayam, E., Wagner, C., Rinaldi, B., Kretz, P.F., Tilly, P., Roos, M., McGillewie, L., Bar, S., Minocha, S*., et al.* (2017). WD40-repeat 47, a microtubule-associated protein, is essential for brain development and autophagy. Proc Natl Acad Sci U S A *114*, E9308-E9317.

Kapitein, L.C., and Hoogenraad, C.C. (2015). Building the Neuronal Microtubule Cytoskeleton. Neuron *87*, 492-506.

Khakshour, S., Beischlag, T.V., Sparrey, C., and Park, E.J. (2015). Probing mechanical properties of Jurkat cells under the effect of ART using oscillating optical tweezers. PLoS One *10*, e0126548.

Kim, M.J., and Maly, I.V. (2009). Deterministic mechanical model of T-killer cell polarization reproduces the wandering of aim between simultaneously engaged targets. PLoS Comput Biol *5*, e1000260.

Kotak, S., and Gonczy, P. (2013). Mechanisms of spindle positioning: cortical force generators in the limelight. Curr Opin Cell Biol *25*, 741-748.

Kreft, K.L., van Meurs, M., Wierenga-Wolf, A.F., Melief, M.J., van Strien, M.E., Hol, E.M., Oostra, B.A., Laman, J.D., and Hintzen, R.Q. (2014). Abundant kif21b is associated with accelerated progression in neurodegenerative diseases. Acta Neuropathol Commun *2*, 144.

Kupfer, A., Dennert, G., and Singer, S.J. (1983). Polarization of the Golgi apparatus and the microtubule-organizing center within cloned natural killer cells bound to their targets. Proc Natl Acad Sci U S A *80*, 7224-7228.

Laan, L., Pavin, N., Husson, J., Romet-Lemonne, G., van Duijn, M., Lopez, M.P., Vale, R.D., Julicher, F., Reck-Peterson, S.L., and Dogterom, M. (2012). Cortical dynein controls microtubule dynamics to generate pulling forces that position microtubule asters. Cell *148*, 502-514.

Labonte, D., Thies, E., and Kneussel, M. (2014). The kinesin KIF21B participates in the cell surface delivery of gamma2 subunit-containing GABAA receptors. Eur J Cell Biol *93*, 338-346.

Letort, G., Nedelec, F., Blanchoin, L., and Thery, M. (2016). Centrosome centering and decentering by microtubule network rearrangement. Mol Biol Cell *27*, 2833-2843.

Li, N., Ma, J., Li, K., Guo, C., and Ming, L. (2017). Different Contributions of CDKAL1, KIF21B, and LRRK2/MUC19 Polymorphisms to SAPHO Syndrome, Rheumatoid Arthritis, Ankylosing Spondylitis, and Seronegative Spondyloarthropathy. Genet Test Mol Biomarkers *21*, 122-126.

Liu, X., Kapoor, T.M., Chen, J.K., and Huse, M. (2013a). Diacylglycerol promotes centrosome polarization in T cells via reciprocal localization of dynein and myosin II. Proc Natl Acad Sci U S A *110*, 11976-11981.

Liu, Y., Zhang, H., Li, J., Zhao, H., Xin, Q., Shan, S., Dang, J., Bian, X., and Liu, Q. (2013b). Association of common variants in KIF21B and ankylosing spondylitis in a Chinese Han population: a replication study. Immunogenetics *65*, 835-839.

Marszalek, J.R., Weiner, J.A., Farlow, S.J., Chun, J., and Goldstein, L.S. (1999). Novel dendritic kinesin sorting identified by different process targeting of two related kinesins: KIF21A and KIF21B. J Cell Biol *145*, 469-479.

Martin-Cofreces, N.B., Robles-Valero, J., Cabrero, J.R., Mittelbrunn, M., Gordon-Alonso, M., Sung, C.H., Alarcon, B., Vazquez, J., and Sanchez-Madrid, F. (2008). MTOC translocation modulates IS formation and controls sustained T cell signaling. J Cell Biol *182*, 951-962.

Martin, M., Veloso, A., Wu, J., Katrukha, E.A., and Akhmanova, A. (2018). Control of endothelial cell polarity and sprouting angiogenesis by non-centrosomal microtubules. Elife *7*.

Meiring, J.C.M., Shneyer, B.I., and Akhmanova, A. (2020). Generation and regulation of microtubule network asymmetry to drive cell polarity. Curr Opin Cell Biol *62*, 86-95.

Mohan, R., Katrukha, E.A., Doodhi, H., Smal, I., Meijering, E., Kapitein, L.C., Steinmetz, M.O., and Akhmanova, A. (2013). End-binding proteins sensitize microtubules to the action of microtubule-targeting agents. Proc Natl Acad Sci U S A *110*, 8900-8905.

Morikawa, M., Tanaka, Y., Cho, H.S., Yoshihara, M., and Hirokawa, N. (2018). The Molecular Motor KIF21B Mediates Synaptic Plasticity and Fear Extinction by Terminating Rac1 Activation. Cell Rep *23*, 3864-3877.

Muhia, M., Thies, E., Labonte, D., Ghiretti, A.E., Gromova, K.V., Xompero, F., Lappe-Siefke, C., Hermans-Borgmeyer, I., Kuhl, D., Schweizer, M.*, et al.* (2016). The Kinesin KIF21B Regulates Microtubule Dynamics and Is Essential for Neuronal Morphology, Synapse Function, and Learning and Memory. Cell Rep *15*, 968-977.

Nath, S., Christian, L., Tan, S.Y., Ki, S., Ehrlich, L.I., and Poenie, M. (2016). Dynein Separately Partners with NDE1 and Dynactin To Orchestrate T Cell Focused Secretion. J Immunol *197*, 2090-2101.

Nedelec, F., and Foethke, D. (2007). Collective Langevin dynamics of flexible cytoskeletal fibers. New Journal of Physics *9*, 427-427.

Noordstra, I., and Akhmanova, A. (2017). Linking cortical microtubule attachment and exocytosis. F1000Res *6*, 469.

Ohashi, K.G., Han, L., Mentley, B., Wang, J., Fricks, J., and Hancock, W.O. (2019). Load-dependent detachment kinetics plays a key role in bidirectional cargo transport by kinesin and dynein. Traffic *20*, 284-294.

Pan, W., Sun, K., Tang, K., Xiao, Q., Ma, C., Yu, C., and Wei, Z. (2018). Structural insights into ankyrin repeat-mediated recognition of the kinesin motor protein KIF21A by KANK1, a scaffold protein in focal adhesion. J Biol Chem *293*, 1944-1956.

Parsey, M.V., and Lewis, G.K. (1993). Actin polymerization and pseudopod reorganization accompany anti-CD3-induced growth arrest in Jurkat T cells. J Immunol *151*, 1881-1893.

Robinson, P.C., Claushuis, T.A., Cortes, A., Martin, T.M., Evans, D.M., Leo, P., Mukhopadhyay, P., Bradbury, L.A., Cremin, K., Harris, J.*, et al.* (2015). Genetic dissection of acute anterior uveitis reveals similarities and differences in associations observed with ankylosing spondylitis. Arthritis Rheumatol *67*, 140-151.

Roig-Martinez, M., Saavedra-Lopez, E., Casanova, P.V., Cribaro, G.P., and Barcia, C. (2019). The MTOC/Golgi Complex at the T-Cell Immunological Synapse. Results Probl Cell Differ *67*, 223-231.

Roostalu, J., Thomas, C., Cade, N.I., Kunzelmann, S., Taylor, I.A., and Surrey, T. (2020). The speed of GTP hydrolysis determines GTP cap size and controls microtubule stability. Elife *9*, e51992.

Samora, C.P., Mogessie, B., Conway, L., Ross, J.L., Straube, A., and McAinsh, A.D. (2011). MAP4 and CLASP1 operate as a safety mechanism to maintain a stable spindle position in mitosis. Nat Cell Biol *13*, 1040-1050.

Santos, A.M., Ponjavic, A., Fritzsche, M., Fernandes, R.A., de la Serna, J.B., Wilcock, M.J., Schneider, F., Urbancic, I., McColl, J., Anzilotti, C.*, et al.* (2018). Capturing resting T cells: the perils of PLL. Nat Immunol *19*, 203-205.

Semenova, I., Ikeda, K., Resaul, K., Kraikivski, P., Aguiar, M., Gygi, S., Zaliapin, I., Cowan, A., and Rodionov, V. (2014). Regulation of microtubule-based transport by MAP4. Mol Biol Cell *25*, 3119-3132.

Seo, M., Lee, S.O., Kim, J.H., Hong, Y., Kim, S., Kim, Y., Min, D.H., Kong, Y.Y., Shin, J., and Ahn, K. (2016). MAP4-regulated dynein-dependent trafficking of BTN3A1 controls the TBK1-IRF3 signaling axis. Proc Natl Acad Sci U S A *113*, 14390-14395.

Serrador, J.M., Cabrero, J.R., Sancho, D., Mittelbrunn, M., Urzainqui, A., and Sanchez-Madrid, F. (2004). HDAC6 deacetylase activity links the tubulin cytoskeleton with immune synapse organization. Immunity *20*, 417-428.

Stepanova, T., Slemmer, J., Hoogenraad, C.C., Lansbergen, G., Dortland, B., De Zeeuw, C.I., Grosveld, F., van Cappellen, G., Akhmanova, A., and Galjart, N. (2003). Visualization of microtubule growth in cultured neurons via the use of EB3-GFP (end-binding protein 3-green fluorescent protein). J Neurosci *23*, 2655-2664.

Stinchcombe, J.C., Majorovits, E., Bossi, G., Fuller, S., and Griffiths, G.M. (2006). Centrosome polarization delivers secretory granules to the immunological synapse. Nature *443*, 462-465.

Tas, R.P., Chen, C.Y., Katrukha, E.A., Vleugel, M., Kok, M., Dogterom, M., Akhmanova, A., and Kapitein, L.C. (2018). Guided by Light: Optical Control of Microtubule Gliding Assays. Nano Lett *18*, 7524-7528.

Traboulsi, E.I., and Engle, E.C. (2004). Mutations in KIF21A are responsible for CFEOM1 worldwide. Ophthalmic Genet *25*, 237-239.

van der Vaart, B., van Riel, W.E., Doodhi, H., Kevenaar, J.T., Katrukha, E.A., Gumy, L., Bouchet, B.P., Grigoriev, I., Spangler, S.A., Yu, K.L.*, et al.* (2013). CFEOM1-associated kinesin KIF21A is a cortical microtubule growth inhibitor. Dev Cell *27*, 145-160.

van Riel, W.E., Rai, A., Bianchi, S., Katrukha, E.A., Liu, Q., Heck, A.J., Hoogenraad, C.C., Steinmetz, M.O., Kapitein, L.C., and Akhmanova, A. (2017). Kinesin-4 KIF21B is a potent microtubule pausing factor. Elife *6*, e24746.

Varga, V., Helenius, J., Tanaka, K., Hyman, A.A., Tanaka, T.U., and Howard, J. (2006). Yeast kinesin-8 depolymerizes microtubules in a length-dependent manner. Nat Cell Biol *8*, 957-962.

Weng, Z., Shang, Y., Yao, D., Zhu, J., and Zhang, R. (2018). Structural analyses of key features in the KANK1.KIF21A complex yield mechanistic insights into the cross-talk between microtubules and the cell cortex. J Biol Chem *293*, 215-225.

Yamada, K., Andrews, C., Chan, W.M., McKeown, C.A., Magli, A., de Berardinis, T., Loewenstein, A., Lazar, M., O'Keefe, M., Letson, R.*, et al.* (2003). Heterozygous mutations of the kinesin KIF21A in congenital fibrosis of the extraocular muscles type 1 (CFEOM1). Nat Genet *35*, 318-321.

Yang, X., Li, M., Wang, L., Hu, Z., Zhang, Y., and Yang, Q. (2015). Association of KIF21B genetic polymorphisms with ankylosing spondylitis in a Chinese Han population of Shandong Province. Clin Rheumatol *34*, 1729-1736.

Yau, K.W., van Beuningen, S.F., Cunha-Ferreira, I., Cloin, B.M., van Battum, E.Y., Will, L., Schatzle, P., Tas, R.P., van Krugten, J., Katrukha, E.A.*, et al.* (2014). Microtubule minus-end binding protein CAMSAP2 controls axon specification and dendrite development. Neuron *82*, 1058-1073.

Yi, J., Wu, X., Chung, A.H., Chen, J.K., Kapoor, T.M., and Hammer, J.A. (2013). Centrosome repositioning in T cells is biphasic and driven by microtubule end-on capture-shrinkage. J Cell Biol *202*, 779-792.

Yue, Y., Blasius, T.L., Zhang, S., Jariwala, S., Walker, B., Grant, B.J., Cochran, J.C., and Verhey, K.J. (2018). Altered chemomechanical coupling causes impaired motility of the kinesin-4 motors KIF27 and KIF7. J Cell Biol *217*, 1319-1334.

Zyss, D., Ebrahimi, H., and Gergely, F. (2011). Casein kinase I delta controls centrosome positioning during T cell activation. J Cell Biol *195*, 781-797.

Figure legends

Figure 1. Immunological synapse formation is impaired in KIF21B-KO Jurkat T cells

A-B) Schematic representation of T cells forming an immunological synapse upon target recognition. In vivo, T cells recognize an antigen-presenting cell (APC) via the T cell receptor (CD3)-complex which triggers T cell activation. Upon activation, several organelles including lysosomes are transported to the centrosome by dynein. Simultaneously, the centrosome and its associated organelle cluster polarize to the synapse through MT pulling by membrane-anchored dynein at the synapse. B) To achieve spatiotemporal control on T cell activation we used anti-CD3 coated glass surfaces to mimic the APC and induce T cell activation and centrosome polarization.

C) Western blot analysis of the indicated Jurkat knockout (KO) cell lines with indicated antibodies. KIF21B-KO clone #1 and #2 were transduced with a KIF21B-GFP construct to generate two polyclonal cell lines re-expressing full-length KIF21B.

D) Phalloidin staining to show F-actin structures in indicated Jurkat T cell lines. Cells were added to poly-D-lysine-coated coverslips with immobilized anti-CD3, fixed after 10 min incubation and imaged on a widefield microscope.

E) Quantification of synapse size expressed as surface area based on a F-actin staining of indicated Jurkat T cells. n = 134, 218, 241, 185 and 194 cells from three independent experiments. ** $p = 0.0098$, *** $p < 0.001$, ns = not significant (Mann-Whitney U test).

F) Immunostaining of Jurkat T cells showing two examples of MT organization at the immunological synapse. Cells were added to poly-D-lysine-coated coverslips with immobilized anti-CD3 and fixed 10 min after incubation. Cells were stained for α-tubulin and CEP135 and were imaged on a TIRF microscope.

G) Quantification of MT organization at immunological synapses. Cells were scored per condition either as “radial” or “disorganized” depending their MT organization as shown in Fig 1E. n = 4, 4, 4, 3 and 3 experiments. In total, 373, 389, 306, 367 and 354 cells were quantified per condition. From left to right: ** $p = 0.0023$, ** $p = 0.0099$, ns = not significant (t test).

H) Confocal images of a non-activated Jurkat T cell on a poly-D-lysine-coated coverslip (without anti-CD3) stained for Lamtor4, F-actin and DAPI. Single Z-plane images (upper panels) show the bottom part of the cell. The position of the single Z-plane images is indicated

in the average intensity z-projection (bottom panels) with a dashed line (orange) labeled with "b" (bottom z-plane).

I) Confocal images of indicated Jurkat T cells. Cells were added to poly-D-lysine-coated coverslips with immobilized anti-CD3 and fixed 10 min after incubation. Cells were stained for Lamtor4, F-actin and DAPI. In addition, the anti-CD3 antibody with which the coverslip was coated was also stained with a Alexa-dye-conjugated secondary antibody. Single Z-plane images (upper panels) show the top part of the cell and the bottom synapse part (indicated in orange). Dashed lines (white) indicated the area of the average intensity Z-projections shown in the bottom panels. The position of the single Z-plane images shown in the upper panels is indicated with dashed lines (orange) labeled with "t" (top z-plane) and "b" (bottom z-plane, synapse).

J-K) Quantification of lysosome positioning relative to the synapse-coverslip interface in indicated conditions. The z-positions of lysosome clusters were analyzed by identifying the peak Lamtor4 fluorescence intensity per cell analyzed from an average intensity side-projection of the cell. Cumulative frequency distribution (J) shows the percentage of cells with fully polarized Lamtor4 clusters. A 2 µm threshold was used to distinguish successful (green area) from failed (red area) Lamtor4 cluster polarization events. Dot plot (K) shows all individual cells quantified in (J). n = 318, 284, 244, 216 and 281 cells from four independent experiments. *** $p < 0.001$, ns = not significant (Mann-Whitney U test).

Figure 2. Knockout of KIF21B causes MT overgrowth in Jurkat cells

A-B) STED images of indicated Jurkat T cell lines. Cells were added to poly-D-lysine-coated coverslips with immobilized anti-CD3 and fixed 7 min after incubation. Cells were stained for α-tubulin and F-actin. Orange boxes indicate zoomed areas shown on the right. (B) Images were background subtracted and split into radial and non-radial components based on the MT orientation in relation to the centrosome. Radial intensity profiles were made from a 45 degree sector starting from the centrosome and directed towards the farthest removed portion of the cell periphery (white). The resulting heat maps were used to quantify the proportion of non-radially oriented MTs as described in Methods.

C) Quantification of the proportion of non-radially oriented MTs analyzed per cell. n = 44, 45 and 52 cells from three independent experiments. *** $p < 0.001$, ns = not significant (t test).

D-E) Volume renderings of indicated T cell lines stained for α-tubulin. T cells were fixed 2 min after activation on poly-D-lysine-coated coverslips with immobilized anti-CD3. Samples were expanded ~4.5 times following an ExM protocol and MTs were imaged using on a confocal microscope. Imaris software was used to create volume renders and analysis. MTs emanating from the centrosome were analyzed using a spherical shell with a 10 μm inner diameter and a thickness of 1 μm (grey); filaments crossing the sphere are highlighted (red). Zooms of the centrosome are shown from two different angles. (E) Fluorescence signal was converted to a surface mask using Imaris software to analyze total tubulin intensity. Additional examples are shown in Figure 2 – figure supplement 1B.

F) Quantification of the total number of MTs per cell emanating from the centrosome quantified at 5 μm distance from the centrosome of indicated Jurkat T cell lines. n = 8 cells for all conditions. From left to right: * p = 0.0131, * p = 0.0367, ns = not significant (t test).

G) Quantification of estimated MT length per cell in indicated Jurkat T cell lines. Fluorescence intensity of 1 μm filament length was measured for all MTs crossing a spherical shell of 1 um width with a 5 μm inner radius located around the centrosome, as shown in Figure 2D. The average MT length per cell was calculated by correcting the total fluorescence intensity per cell by the number of MTs at the centrosome. n = 8 cells for all conditions. *** p = 0.0002, ** p = 0.0013, ns = not significant (t test).

Figure 3. KIF21B induces MT pausing and catastrophes in T cells

A) Live imaging of indicated Jurkat KIF21B-KO T cells stably overexpressing KIF21B-GFP on Lab-Tek chambered coverglass with immobilized anti-CD3. Images show a single movie frame and a maximum intensity projection of a background-subtracted movie. Zoomed areas are indicated (orange), and the kinesin track corresponding to the kymograph shown is indicated with red arrowheads.

B) Frequency distribution of KIF21B-GFP velocity in cells measured from data obtained imaging of KIF21B-KO #2 Jurkat T cell line stably overexpressing KIF21B-GFP on a TIRF microscope at 10 fps. Velocities were measured by kymograph analysis and the numbers were fitted to a Gaussian (red curve). n = 464 events from 102 cells from four independent experiments.

C) Histograms (dots) of peak-fitted fluorescence intensities of monomeric GFP immobilized on glass (green dots) and KIF21B-GFP motors imaged in Jurkat T cells (blue/orange) in two separate chambers on the same coverslip and the corresponding lognormal fits (solid lines). Imaging conditions were identical for both samples. KIF21B-GFP intensity values were corrected for a 50 and 75 nm distance from the coverslip, as illustrated in Figure 3 - figure supplement 1B. n = 2601 (GFP) and n = 16523 (6 cells) (KIF21B-GFP) molecules. Mean values relative to monomeric GFP are indicated in the plot.

D-I) Live-cell imaging of KIF21B-KO #2 Jurkat T cell line stably overexpressing KIF21B-GFP and transiently overexpressing EB3-mCherry to label growing MT plus ends. Cells were added on Lab-Tek chambered coverglass with immobilized anti-CD3 and imaged on a TIRF microscope at 10 fps.

D) Kymographs illustrating KIF21B-GFP motors switching from walking to a pausing state. Growing MTs are visualized by EB3-mCherry overexpression. Examples show a growing plus end that undergoes pausing after KIF21B-GFP arrival followed by a catastrophe event (left), or growth re-initiation when the pausing KIF21B-GFP dissociates (middle). Some plus ends are not affected by the KIF21B-GFP motor pause event (right).

E) Kymograph illustrating a KIF21B-GFP tip-tracking on a growing EB3-mCherry plus end followed by a pausing event of both KIF21B-GFP and the MT plus end.

F) Kymograph illustrating two KIF21B-GFP motors reaching a growing EB3-mCherry plus-end causing the motors to dissociate from the MT plus-end, which continues growing, though EB3-mCherry signal is reduced.

G) Quantification of KIF21B-GFP fates observed when a moving KIF21B motor reaches an EB3-mCherry-labeled MT plus end, as illustrated in Figure 3D-F. n = 224 events from two independent experiments.

H) Quantification of MT plus-end fates when a KIF21B-GFP motor reaches a growing EB3-mCherry-labeled MT plus end and transitions to a paused state, as illustrated in Figure 3D,E, Figure 3 - figure supplement 1C. n = 149 events from two independent experiments.

I) Quantification of pause duration of KIF21B-GFP and EB3-mCherry-labeled MT plus ends, illustrated in Figure 3G and H. n = 144 and 75 events from two independent experiments.

Figure 4. Mild inhibition of MT growth with vinblastine rescues centrosome repositioning in KIF21B-KO cells

A) Live-cell imaging of indicated EB3-GFP overexpressing Jurkat T cell lines. Cells were added to Lab-Tek chambered coverglass with immobilized anti-CD3 and imaged on a TIRF microscope at 2.5 fps. Color-coded maximum intensity projections and illustrative kymographs of growing EB3-GFP comets are shown per condition. KIF21B-KO cells were untreated or treated with 0.5 nM vinblastine 30 min prior to imaging as indicated. A scale for the time-dependent color-coding is indicated on the right.

B) Quantification of MT growth rates determined from imaging EB3-GFP in indicated Jurkat T cell lines. Dashed line (magenta) indicates the average growth rate for control cells. n = 470, 478, 250, 255 and 267 events from three independent experiments. ** $p = 0.0024$, *** $p < 0.001$, ns = not significant (Mann-Whitney U test).

C) Quantification of MT catastrophe frequencies determined from imaging EB3-GFP in indicated Jurkat T cell lines. Dashed line (magenta) indicates the average catastrophe frequency for control cells. n = 178, 178, 170, 205 and 173 events from two independent experiments. ** $p = 0.0029$, *** $p < 0.001$, ns = not significant (Mann-Whitney U test).

D) Live-cell imaging of β-tubulin-GFP overexpressing Jurkat T cell lines. Cells were added on Lab-Tek chambered coverglass with immobilized anti-CD3 and imaged on a TIRF microscope at 10 fps. Movie stills and kymographs show examples of MTs that undergo sliding (pink arrowheads), buckling (cyan arrowheads), pausing (green arrowheads) or catastrophe (red arrowheads) after reaching the cell periphery. Yellow arrowheads indicate growing MTs before the highlighted events take place. Kymographs show the corresponding MT pausing and catastrophe events; the catastrophe initiation (red arrowhead) and total pause time (green line) are indicated.

E) Quantification of MT plus-end fates after reaching the cell periphery based on live-cell imaging of indicated β-tubulin-GFP overexpressing Jurkat T cell lines. n = 518, 508, 477, 544 and 409 events from 46, 49, 38, 37 and 32 cells obtained from three independent experiments.

F) Cumulative frequency distribution shows pause duration of events quantified in Figure 4E based on live-cell imaging of indicated β-tubulin-GFP overexpressing Jurkat T cell lines. A quantification of these data is shown in Figure 4 – figure supplement 1A. n = 229, 110, 114,

117 and 101 events from 46, 49, 38, 37 and 32 cells obtained from three independent experiments.

G) Confocal images of indicated Jurkat T cells. Cells were added to poly-D-lysine-coated coverslips with immobilized anti-CD3 and fixed 10 min after incubation. Cells were stained for CEP135, F-actin and DAPI. In addition, the anti-CD3 antibody with which the coverslip was coated was also stained with a Alexa-dye-conjugated secondary antibody. Single Z-plane images (upper panels) show the top part of the cell and the bottom synapse part. White dashed lines indicate the position of the average intensity Z-projections shown in the bottom panels. Yellow arrowheads indicate the position of the CEP135-positive centriole staining. The positions of the single Z-plane images shown in the upper panels are indicated with dashed lines (orange) labeled with "t" (top z-plane) and "b" (bottom z-plane, synapse).

H-I) Quantification of CEP135 distance from the synapse-coverslip interface for indicated conditions. Cumulative frequency distribution (H) shows the percentage of cells with fully polarized centrosomes. A 2 µm threshold was used to distinguish successful (green area) from failed (red area) centrosome polarization events. Dot plot (I) shows the distance values for individual cells quantified in (H). n = 109, 119, 132, 150, 150, 133 and 175 cells from three independent experiments. Comparison with control (black stars): * $p = 0.0187$, *** $p < 0.001$, ns = not significant (Mann-Whitney U test). Comparison with related KIF21B KO condition (grey stars): ** $p = 0.0042$, *** $p < 0.001$, ns = not significant (Mann-Whitney U test).

Figure 5. Biophysical simulation shows how KIF21B affects MT network length

A) A T cell is modeled as a circular cell with a nucleus (light blue) and centrosome confinement space (red). The cell is 14 µm in diameter, the nucleus is 10 µm in diameter.

B) Description of modelled microtubule dynamics using two models: a non-pausing model with MTs undergoing force-dependent growth and transitioning to depolymerization stochastically with a constant catastrophe rate, and a KIF21B-pausing model, in which MT growth and catastrophe are dependent on the antagonistic force exerted on the fiber's tip. Cropped snapshots of the initial state of the non-pausing model (left, catastrophe rate = 0.045 s^{-1}) and KIF21B-pausing model (right, 10 KIF21B motors) are shown. Growing MT plus ends are indicated by yellow arrowheads, depolymerizing MT plus ends are indicated by red arrowheads, and KIF21B units by orange circles.

C) Snapshots of the non-pausing model after 300 s for different values of catastrophe rate: 0.02 s^{-1} (left), 0.045 s^{-1} (middle) and 0.07 s^{-1} (right).

D) Trajectories (left) showing mean MT length per simulated cell over a 300 s time period. Traces are colored according to the catastrophe rate (from k_{cat} = 0.02 to 0.07 s^{-1}). Quantification (right) displaying mean MT length per simulated cell at steady state (t = 300 s) for indicated values of the catastrophe rate (k_{cat}). n = 30 simulated cells per condition.

E) Snapshots of the KIF21B-pausing model after 300 s for different numbers of KIF21B motors: 0 (left), 4 (middle), and 10 (right).

F) Trajectories (left) showing mean MT length per simulated cell over a 300 s time period. Traces are colored according to the number of KIF21B motors present (ranging from 0 to 10 motors). Quantification (right) displaying mean MT length per simulated cell at steady state (t = 300 s) for indicated number of KIF21B motors. n = 30 simulated cells per condition.

Figure 6. KIF21B prevents centrosome stalling induced by force balance during polarization by limiting MT length

A) The T cell model is initialized to a steady state MT network in 300 s (Phase I) and is then extended to a polarizing model (Phase II). In this transition, the cell shape is changed to include a flat side with curved corners with 50 dynein units attached, and the centrosome confinement (red) is released to allow centrosome movement and translocation.

B) Snapshots of modelled T cells during centrosome polarization in the KIF21B-pausing model with the presence of 10 (top row) or 0 (bottom row) KIF21B motors. The simulations were stopped after the centrosomes reached a polarized position < 2.5 µm away from the synapse. The final snapshot in each row indicates the frame of the simulation when the centrosome was fully polarized. Timepoints are indicated below each snapshot.

C) Quantification of polarization time (the time the centrosome needs in Phase II to reach a polarization position) per simulated cell for the non-pausing model at indicated catastrophe rates. Some cells did not polarize within the maximum simulation time (800 s) as indicated in the upper part of the graph. n = 30 simulated cells per condition.

D) Quantification of polarization time (the time the centrosome needs in Phase II to reach a polarization position) per simulated cell for the KIF21B-pausing model with indicated numbers

of KIF21B motors present. Some cells did not polarize within the maximum simulation time (800 s) as indicated in the upper part of the graph. n = 30 simulated cells per condition.

E) Trajectories showing the centrosome-synapse distance during Phase II over time along the vertical axis of the simulated T cell. Trajectories are color coded for the number of KIF21B motors present (see legend). Shown are 15 runs per condition.

F) Quantification of force imbalance within the KIF21B-pausing model. Force imbalance is calculated from the forces experienced by dynein at a given time point, projected on the horizontal axis. Force imbalance was characterized as the absolute difference of projected forces pointing to the left and forces pointing to the right, normalized by the sum of all forces. This quantity is determined for each timestep between 0 and the polarization time for every repeat and binned to create the according histogram. Histograms are color coded for the number of KIF21B motors present in the simulation (see legend). n = 30 simulated cells per condition.

G) Quantification of the mean number of MTs that are bound by dynein to the synapse within the KIF21B-pausing model. Violin plot distributions show the total number of MTs bound (purple), and the absolute difference ($|MT_L-MT_R|$, yellow) between the number of MTs bound on the right versus left side of the cell's vertical axis. Within each violin, a boxplot indicates the quartiles (black) with the inner quartile range (25 – 75%) indicated with the thickened region. Median values are indicated for each violin (white dot). Values were obtained in the first 10 s of Phase II of each simulation. n = 30 simulated cells per condition.

H) Trajectories of centrosome-synapse distance over time (solid lines) plotted together with trajectories of the absolute difference $|MT_L-MT_R|$ between the number of MT bound to dynein and passing the nucleus on the left or on the right (dashed lines). in the same color for the corresponding runs. To make the $|MT_L-MT_R|$ more legible, the mean and 95% confidence interval is plotted averaged over 3 frames (1.2 s). Trajectories are color coded for the number of KIF21B motors present in the simulation (see legend).

Figure 7. Overview of the experimental results and a model of centrosome polarization in T cells

Centrosome polarization in T cells is driven by dynein attached to the immunological synapse. KIF21B is a pausing and catastrophe-promoting factor that limits MT growth in T cells; its depletion results in MT overgrowth. Cells with overly long MTs experience difficulties in

centrosome polarization. Re-expression of KIF21B-GFP or the application of a low-dose of MT-targeting agent vinblastine restores the centrosome polarization. Computational modelling suggests that an imbalance in MT pulling forces drives the centrosome movement along the nucleus. Overly long MTs create additional connections to the synapse, resulting in a balance of pulling forces on the two sides of the nucleus, thereby hindering centrosome translocation. Overly long MTs may also directly inhibit force generation by dynein at the synapse.

Legends to Supplemental Figures

Figure 1 – figure supplement 1

Scans of Western blot images corresponding to Figure 1C. Areas used in Figure 1C are highlighted per blot (red). High exposure images for anti-tubulin and anti-Ku80 blots are included to make the blot background visible.

Figure 1 – figure supplement 2. Characterization of KIF21B knockout cell lines.

A-B) qRT-PCR measurements of IL-2 expression levels after stimulation at indicated timepoints. Indicated Jurkat T cell lines were treated with 2 ng/ml PMA and 100 ng/ml ionomycin (A, mild stimulation) or 20 ng/ml PMA and 1 µg/ml ionomycin (B, strong stimulation), after which RNA was isolated and cDNA was generated. IL-2 expression was measured by qRT-PCR, and values were normalized to GAPDH levels. IL-2 expression is shown in a log10 scale.

C) Volume rendering of indicated Jurkat T cells. Cells were added to poly-D-lysine-coated coverslips with immobilized anti-CD3 and fixed 10 min after incubation. Cells were stained for F-actin (using phalloidin). Side views (top panel row) and angled views (middle and bottom row) are indicated. Cell volume was measured by converting F-actin fluorescence signal to a surface mask using Imaris software (isoline tool). xyz dimensions correspond to 2 µm per block on the displayed grid.

D) Quantification of T cell volumes based on F-actin staining. n = 33, 34 and 34 cells from three independent experiments, ns = not significant (Mann-Whitney U test).

E) Live-cell imaging of indicated Jurkat T cells forming immunological synapses on Lab-Tek chambered coverglass with immobilized anti-CD3, imaged on a widefield microscope using DIC microscopy at 2.5 s per frame interval. Green boxed stills indicate start of synapse formation, orange boxed stills show fully formed synapses at their maximum size. Dotted line in the first movie still indicates the position of the kymograph in Figure 1 – figure supplement 2F.

F) Kymographs of immunological synapse formation corresponding to the movie stills shown in Figure 1 – figure supplement 2E. Landing of the Jurkat T cell on the anti-CD3 coated glass

surface is marked by the pink asterisk. The start of synapse formation (Start) is indicated in green, the moment a synapse reaches its maximum size is indicated in orange (Max) and the white bar indicates time between Start and Max.

G) Quantification of spreading time. n = 87, 107 and 91 cells from two independent experiments. *** p = 0.0009, ** p = 0.0018, ns = not significant (Mann-Whitney U test).

H) Immunostaining of Jurkat T cells incubated on poly-D-lysine coated coverslips coated without or with indicated antibodies. Cells were stained for CEP135 and the bottom part of these cells were imaged on a TIRF microscope.

I) Quantification of centrosome localization in T cells after incubation on indicated coated surfaces. Cells were scored for the presence of CEP135-staining at the imaged TIRF plane indicating centrosome polarization. n = 4 experiments for all conditions. In total, 354, 310 and 311 cells were quantified per condition.

Figure 2 – figure supplement 1. Characterization of MT network in polarizing T cells by ExM.

A) Quantification of total estimated MT length per cell indicated in indicated Jurkat T cell lines. Values were obtained by multiplication of total MT numbers by the estimated average MT length per cell. n = 8 cells for all conditions. * p = 0.0169, ** p = 0.0043, ns = not significant (t test).

B) Series of 5 exemplary volume renderings per indicated T cell lines stained for α-tubulin (related to Figure 2D, E). T cells were fixed 2 min after activation on poly-D-lysine-coated coverslips with immobilized anti-CD3. Samples were expanded ~4.5 times following an ExM protocol and MTs were imaged using on a confocal microscope. Imaris software was used to create volume renders.

C) Volume renderings of indicated T cell lines stained for α-tubulin to highlight examples suggesting that a MT stalk is formed during the process of centrosome polarization. Centrosome (cyan arrowheads) and MT stalks emanating from the centrosome towards the synapse are indicated (orange arrowheads).

Figure 3 – figure supplement 1. Characterization of KIF21B motility in cells.

A) Workflow for GFP (monomer reference) and KIF21B-GFP single molecule counting. Imaging was performed in a dual-chamber microscope slide in a single imaging session with identical microscope settings. Monomeric GFP was expressed in HEK293T cells and lysates were diluted in PBS to single molecule densities in the first chamber. KIF21B-KO #2 Jurkat T cell line with stable overexpression of KIF21B-GFP were added to the second chamber, which was coated with anti-CD3 antibodies. Single molecules were detected using DoM ImageJ plugin and for KIF21B-GFP motors in cells, single molecules were only analyzed from kinesin tracks with a duration of > 1 s.

B) Lognormal fits of peak-fitted fluorescence intensities of monomeric GFP immobilized on glass (green dots) and KIF21B-GFP motors imaged in Jurkat T cells corrected for a hypothetical range of distances between molecule and coverslip. The evanescent field decays exponentially and KIF21B-GFP fluorescence is corrected for that given the TIRF laser angle was fixed at a penetration depth d of 180 nm.

C) Kymograph illustrating KIF21B-GFP motors switching from walking to a pausing state. Growing MT end is visualized with EB3-mCherry. A static plus end undergoes a catastrophe after a KIF21B-GFP pausing event (right).

D) Quantification of MT plus-end state when a KIF21B-GFP motor reaches the EB3-mCherry-labeled MT plus end and transitions to a paused state, as illustrated in Figure 3D and Figure 3 – figure supplement 1C. Numbers relate to the “Pausing” and “Tip-tracking + pausing” category of Figure 3G. n = 149 events from two independent experiments.

E) Kymographs illustrating a KIF21B-GFP motor reaching a growing EB3-mCherry MT plus end where motor dissociation from the MT coincides with MT pausing (left) or a catastrophe event (right).

F) Quantification of MT plus-end fate when a KIF21B-GFP motor reaches a growing EB3-mCherry labeled plus-end and dissociates, as illustrated in Figure 3F, Figure 3 – figure supplement 1E. n = 75 events from two independent experiments.

G) Kymograph illustrating a KIF21B-GFP motor directly associating to an EB3-mCherry labeled growing MT plus end and affecting MT growth until KIF21B-GFP dissociates.

Figure 4 – figure supplement 1. KIF21B-depleted cells lack long MT pause events.

A) Quantification of MT pause duration as shown in Figure 4F based on live-cell imaging of indicated β-tubulin-GFP overexpressing Jurkat T cell lines. Pause durations are derived from MT pausing events described in Figure 4D and E. n = 229, 110, 114, 117 and 101 events from 46, 49, 38, 37 and 32 cells obtained from three independent experiments. *** $p < 0.001$, ns = not significant (Mann-Whitney U test).

B) STED images of indicated Jurkat T cell lines. Cells were added to poly-D-lysine-coated coverslips with immobilized anti-CD3 and fixed 7 min after incubation. Cells were stained for tubulin.

Figure 5 – figure supplement 1. Characterization of T cell force-dependent catastrophe.

A) Reverse cumulative distribution plot showing MT pause times for KIF21B-KO and control with the immediate catastrophes at t = 0 s. The exponential fit (rate = mean pause time^{-1}) corresponds to a catastrophe rate of 0.3 s^{-1} in the KIF21B-KO and 0.15 s^{-1} in the control. From the assumption that all pausing in the KIF21B-KO cells is from antagonistic force, the stalled catastrophe rate $k_{cat,stall}$ can be set to 0.3 s^{-1}. From this rate follows a characteristic time of 3.33 s (shaded area).

B) To match the parametrization of the MT dynamics to the experimental data, a *Cytosim* model is introduced that describes the fully spread synapse for the KO condition. The space is meant to model the TIRF data of KIF21B-KO synapses after they have spread, thus the cell has a radius of 9.57 µm and no nucleus. For ease of measurement, the centrosome is fixed in the center of the cell. From the stalled catastrophe rate of 0.3 s^{-1} follows that 63% of all catastrophe events happen in the first 3.33 s. From the experimental data, it is known that only approximately 30% of the counted paused KIF21B-KO MTs (under force) do not buckle or slide, but they are counted into the fraction of catastrophe events. Taking 30% of the 63% gives us 19%: the percentage of catastrophe in 3.33 s. Therefore, we can use the constraint that 81% of MTs survive under force for 3.33 s in our synapse model to match the two-state model to our KIF21B-KO pause times.

C) Graph showing the number of surviving MTs in 3.33 s under force at indicated free-growing catastrophe rates ($k_{cat,free\text{-}growing}$) and characteristic force exerted by the MT polymerization growth (F_{grow}). Measurements (small dots) and linear fits (lines) are color coded for the value

of F_{grow} (see legend). The large dots on the lines indicate the level at which 81% of the MTs survive, taken from the linear fit.

D) Graph showing points (blue) from Figure 5 – figure supplement 1C at which 81% MT survive in the synapse plotted as a function of the free catastrophe rate ($k_{cat,free\text{-}growing}$) and of the growing force (F_{grow}). A catastrophe rate is obtained from a linear fit (orange line) to the realistic, non-negative points, which gives a linear relationship between F_{grow} and $k_{cat,free\text{-}growing}$, where MT dynamics match that the KIF21B-KO cells.

Figure 6 – figure supplement 1. KIF21B affects the balance of force in T cell polarization.

Histogram showing the force on dynein at every timestep. The forces on dynein along the x-axis are summed, where left-pointing forces are taken as negative. This sum is taken for every recorded time between 0 and the polarization time of the simulation and binned to create histograms. Histograms are color coded for the number of KIF21B motors present in the simulation (see legend).

Videos

Video 1. 3D volume render of an ExM imaged Jurkat control cell 2 min after activation.

Volume rendering of a control Jurkat cell fixed 2 min after activation on anti-CD3 coated coverslips stained for α-tubulin. Samples were isotropically expanded using an ExM protocol and imaged on a confocal microscope. Images were processed and analyzed using Imaris software. Microtubules emanating from the centrosome were analyzed using a spherical shell with a 5 µm inner radius, filaments crossing the sphere are highlighted (red). Every square in the grid corresponds to 5 x5 µm post expansion. Example corresponds to Figure 2D-E.

Video 2. 3D volume render of an ExM imaged Jurkat KIF21B-KO cell (KO #1) 2 min after activation.

Volume rendering of a KIF21B-KO Jurkat cell (KO #1) fixed 2 min after activation on anti-CD3 coated coverslips stained for α-tubulin. Samples were isotropically expanded using an ExM protocol and imaged on a confocal microscope. Images were processed and analyzed using Imaris software. Microtubules emanating from the centrosome were analyzed using a spherical shell with a 5 µm inner radius, filaments crossing the sphere are highlighted (red). Every square in the grid corresponds to 5 x5 µm post expansion. Example corresponds to Figure 2D-E.

Video 3. 3D volume render of an ExM imaged Jurkat KIF21B-KO cell (KO #2) 2 min after activation.

Volume rendering of a control KIF21B-KO Jurkat cell (KO #2) fixed 2 min after activation on anti-CD3 coated coverslips stained for α-tubulin. Samples were isotropically expanded using an ExM protocol and imaged on a confocal microscope. Images were processed and analyzed using Imaris software. Microtubules emanating from the centrosome were analyzed using a spherical shell with a 5 µm inner radius, filaments crossing the sphere are highlighted (red). Every square in the grid corresponds to 5 x5 µm post expansion. Example corresponds to Figure 2D-E.

Video 4. KIF21B-GFP motors imaged at the immunological synapse of an activated Jurkat T cell.

Live imaging of a Jurkat KIF21B-KO T cell (KO #2) stably overexpressing KIF21B-GFP. Video corresponds to Figure 3A. Images were collected using a TIRF microscope at 10 frames per second. Video is sped up 2 times to 20 frames per sec. Time is shown in seconds.

Video 5. Recording of a simulated T cell in the 'non-pausing' model with 10 KIF21B motors added.

The T cell simulation consists of two phases. At first, the model is initialized to a steady state MT network in the first 300 s, during which the centrosome is confined to the red box at one side of the T cell. Next, the cell shape is changed to include 50 membrane-anchored dynein motors (blue) at a flat immunological synapse surface, and centrosome confinement is released to allow centrosome translocation. KIF21B motors are included throughout the entire simulation (orange). Snapshots of this run are shown in Figure 6B (upper row). Growing MT plus ends are indicated by yellow arrowheads, depolymerizing MT plus ends are indicated by red arrowheads, and KIF21B units by orange circles.

Video 6. Recording of a simulated T cell in the 'non-pausing' model with 0 KIF21B motors added.

The T cell simulation consists of two phases. At first, the model is initialized to a steady state MT network in the first 300 s, during which the centrosome is confined to the red box at one side of the T cell. Next, the cell shape is changed to include 50 membrane-anchored dynein motors (blue) at a flat immunological synapse surface, and centrosome confinement is released to allow centrosome translocation. Snapshots of this run are shown in Figure 6B (bottom row). Growing MT plus ends are indicated by yellow arrowheads and depolymerizing MT plus ends are indicated by red arrowheads.

Supplemental Table S1. Parameters used for simulations.

Parameter	**Value**	**Description/Reference**
MTs		
Polymerization speed	0.3 µm/s	This study
Depolymerization speed	1 µm/s	This study
Rigidity	20 pN/µm	(Gittes et al., 1993)
Stall force	5 pN	Describes the modulation of growth speed and catastrophe rate by antagonistic force (Dogterom and Yurke, 1997)
Catastrophe rate	0.02 s^{-1}, 0.3 s^{-1}	Matched to TIRF GFP-β-tubulin data (Figure 4D-E)
Cell		
Viscosity	0.1 pN.s/µm^2	Internal viscosity of T cells, like most blood cells, is usually estimated to be lower than that of somatic cells. Jurkat cell internal viscosity has been reported at different values (Daza et al., 2019; Khakshour et al., 2015). Because there is no consensus on the value, we used a viscosity such that the KIF21B-mediated polarization happens within the timescale measured for polarization.

Elasticity	100 pN/µm	The spring stiffness of the cell for all objects with inertia. This same stiffness is used for interaction of MTs with the nucleus
Radius	7 µm	This study, calculated from Figure 1 – figure supplement 2C-D.
Synapse fraction	0.9	This corresponds to a synapse cutting off 10% of the height of the cell (1.4 µm).
Interpolation distance	1 µm	The curvature starts 1 µm under the synapse (at 2.4 µm from the top of the unpolarized cell).
centrosome		
First anchoring stiffness	500 pN/µm	Rotational stiffness on the MTs at the center of the centrosome, as proposed previously (Letort et al., 2016).
Second anchoring stiffness	500 pN/µm	Rotational stiffness on the MTs exerted at the periphery of the centrosome, as proposed previously (Letort et al., 2016).
Number of MTs	90	
Dynein		
Walking speed	1 µm/s	Average value from MT gliding over dynein (Laan et al., 2012)
Number	50	
Stall force	4 pN	(Belyy et al., 2016)

Unbinding rate	1 s^{-1}	(Ohashi et al., 2019)
Initialization	uniform on synapse	Dynein is initialized on the synapse and part of the interpolated curve connecting the synapse to the rest of the cell. The region is defined as being within 1.6 µm of the synapse along the vertical axis.
Link stiffness	100 pN/µm	Describes the elastic stiffness of the link between MT-binding site and anchoring point (Letort et al., 2016)
KIF21B		
Walking speed	0.71 µm/s	This study
MT state after a KIF21B-induced pause	Shrinkage	We inflate the effect of KIF21B to always cause catastrophe in order to more clearly display the effect of KIF21B as a delayed catastrophe inducer.
Capable of pausing a shrinking MT	No	This means that the KIF21B motors do not cooperatively pause: if one of them unbinds, the fiber is set to shrinkage and another bound KIF21B cannot pause this shrinking fiber.
System		
Dimensionality	2D	The overgrown KIF21B-KO MT system requires much computation per timestep, and thus we were not able to expand to 3D and keep our fit of the system.
Number of repeats	30 per condition	In some figures, fewer repeats are shown for readability. If so, the ones were chosen that were run first chronologically, to avoid bias in run selection.

Key Resources Table				
Reagent type (species) or resource	**Designation**	**Source or reference**	**Identifiers**	**Additional information**
Cell line (*Homo sapiens*)	HEK293T	ATCC	CRL-11268	
Cell line (*Homo sapiens*)	Jurkat, Clone E6-1	ATCC	TIB-152	
Cell line (*Homo sapiens*)	Jurkat, KIF21B KO#1	This paper		CRISPR/Cas9 generated monoclonal Jurkat cell line
Cell line (*Homo sapiens*)	Jurkat, KIF21B KO#2	This paper		CRISPR/Cas9 generated monoclonal Jurkat cell line
Cell line (*Homo sapiens*)	Jurkat, KIF21B KO#1, re-expressing KIF21B-GFP	This paper		Polyclonal line re-expressing KIF21B-GFP; generated from monoclonal KIF21B KO#1 Jurkat cells
Cell line (*Homo sapiens*)	Jurkat, KIF21B KO#2, re-expressing KIF21B-GFP	This paper		Polyclonal line re-expressing KIF21B-GFP; generated from monoclonal KIF21B KO#2 Jurkat cells
Cell line (*Homo sapiens*)	Jurkat cells (control), expressing EB3-GFP	This paper		Polyclonal Jurkat (control) line expressing EB3-GFP

Cell line (*Homo sapiens*)	Jurkat, KIF21B KO#1, expressing EB3-GFP	This paper		Polyclonal line expressing EB3-GFP; generated from monoclonal KIF21B KO#1 Jurkat cells
Cell line (*Homo sapiens*)	Jurkat, KIF21B KO#2, expressing EB3-GFP	This paper		Polyclonal line expressing EB3-GFP; generated from monoclonal KIF21B KO#2 Jurkat cells
Cell line (*Homo sapiens*)	Jurkat cells (control), expressing β-tubulin-GFP	This paper		Polyclonal Jurkat (control) line expressing β-tubulin-GFP
Cell line (*Homo sapiens*)	Jurkat, KIF21B KO#1, expressing β-tubulin-GFP	This paper		Polyclonal line expressing β-tubulin-GFP; generated from monoclonal KIF21B KO#1 Jurkat cells
Cell line (*Homo sapiens*)	Jurkat, KIF21B KO#2, expressing β-tubulin-GFP	This paper		Polyclonal line expressing β-tubulin-GFP; generated from monoclonal KIF21B KO#2 Jurkat cells
Transfected construct (*Homo sapiens*)	KIF21B-GFP	This paper		Lentiviral construct to transfect and express KIF21B-GFP in Jurkat cells
Transfected construct (*Homo sapiens*)	EB3-GFP	Bouchet et al., 2016; PMID: 27939686		Lentiviral construct to

				transfect and express EB3-GFP in Jurkat cells
Transfected construct (*Homo sapiens*)	β-tubulin-GFP	Bouchet et al., 2016; PMID: 27939686		Lentiviral construct to transfect and express β-tubulin-GFP in Jurkat cells
Transfected construct (Homo sapiens)	EB3-mCherry	Stepanova et al., 2003; PMID: 12684451		Expression construct transfected in Jurkat cells
Sequence-based reagent	gRNA targeting sequence against KIF21B	This paper	gRNA sequence	caccgTGTGTGAGCAAGCTCATCGA
Sequence-based reagent	GAPDH_fw	This paper	qPCR primer	CAACGGATTTGGTCGTATT
Sequence-based reagent	GAPDH_rev	This paper	qPCR primer	GATGGCAACAATATCCACTT
Sequence-based reagent	IL-2_fw	This paper	qPCR primer	AACTCACCAGGATGCTCACATTTA
Sequence-based reagent	IL-2_rev	This paper	qPCR primer	TCCCTGGGTCTTAAGTGAAAGTTT
Antibody	Anti-CD3, clone UCHT1 (mouse monoclonal)	StemCell Technologies	Cat# #60011	Coverslip coating (10 µg/mL) WB (1:400)

Antibody	Anti-HA, clone 16B12 (mouse monoclonal)	Biolegend (Covance)	Cat# MMS-101P, RRID:AB_10064068	Coverslip coating (10 µg/mL)
Antibody	anti-KIF21B (rabbit polyclonal)	Sigma-Aldrich	Cat# HPA027249, RRID:AB_10602241	WB (1:1000)
Antibody	Anti-GFP (rabbit polyclonal)	Abcam	Cat# Ab290, RRID:AB_303395	WB (1:5000)
Antibody	Anti-Ku80 (mouse monoclonal)	BD Bioscience	Cat# 611360, RRID:AB_398882	WB (1:2000)
Antibody	Anti- Lamtor4, clone D6A4V (rabbit monoclonal)	Cell Signalling Technology	Cat# 12284, RRID:AB_2797870	IF (1:200)
Antibody	anti-CEP135 (rabbit polyclonal)	Sigma-Aldrich	Cat# SAB4503685; RRID:AB_10746232	IF (1:200)
Antibody	Anti- α-tubulin, clone EP1332Y (rabbit monoclonal)	Abcam	Cat# ab52866, RRID:AB_869989	IF (1:250) for ExM samples
Antibody	Anti-α-tubulin (mouse monoclonal	Sigma-Aldrich	Cat# T6199, RRID:AB_477583	IF (1:250) for STED samples WB (1:10000)
Antibody	Anti- α-tubulin, clone γL1/2 (rat monoclonal)	Abcam	Cat# Ab6160, RRID:AB_305328	IF (1:300)

Antibody	Alexa Fluor 488-, 594- and 647-secondaries	Molecular Probes		IF (1:200 – 1:400)
Antibody	IRDye 680LT and 800CW secondaries	Li-Cor Biosciences		WB (1:10000)
Commercial assay or kit	Amaxa Cell Line Nucleofector® kit V	Lonza	Cat# VPB-1002	program X-001 or X-005
Commercial assay or kit	iScript cDNA synthesis kit	Bio-Rad	Cat# 1708891	
Commercial assay or kit	SYBR Select mastermix	Life Technologies	Cat# 44-729-19	
Peptide, recombinant protein	Proteinase-K	Thermo Fisher	Cat# EO0491	
peptide, recombinant protein	Monomeric GFP	This paper		Obtained from HEK293T lysates containing overexpressed eGFP. (Clontech pEGFP-C1 vector)
Chemical compound, drug	acryloyl X-SE (AcX)	Thermo Fisher	Cat# A20770	
Chemical compound, drug	sodium acrylate	Sigma-Aldrich	Cat# 408220	

Chemical compound, drug	AA/BIS solution	Sigma-Aldrich	Cat# A3699	
Chemical compound, drug	BIS	Sigma-Aldrich	Cat# M1533	
Chemical compound, drug	cOmplete protease inhibitor cocktail	Roche	Cat# 4693132001	
Chemical compound, drug	Puromycin	InvivoGen	Cat# ant-pr5b	(2 µg/mL)
Chemical compound, drug	Hygromycin	Invivogen	Cat# ant-hm	(100 µg/mL)
Chemical compound, drug	Polybrene	Merck-Millipore	Cat# TR-1003-G	(8 µg/mL)
Chemical compound, drug	Poly-D-Lysine	Thermo Fisher	Cat# A3890401	
Chemical compound, drug	Vinblastine	Sigma-Aldrich	Cat# V1377	
Chemical compound, drug	Phorbol 12-myristate 13-acetate (PMA)	Sigma-Aldrich	Cat# P8139	
Chemical compound, drug	ionomycin	Sigma-Aldrich	Cat# I0634	

Chemical compound, drug	TRIzol	Thermo Fisher Scientific	Cat# 15596026	
Software, algorithm	GraphPad Prism	GraphPad Prism (https://graphpad.com)	RRID:SCR_015807	
Software, algorithm	FIJI/ImageJ	FIJI/ImageJ (https://imagej.net/Fiji)	RRID:SCR_002285	
Software, algorithm	ImageJ detection of molecules plugin (DoM)	Chazeau et al., 2016; PMID: 26794511		
Software, algorithm	ImageJ KymoResliceWide plugin			https://github.com/ekatrukha/KymoResliceWide
Software, algorithm	ImageJ radiality plugin	Martin et al., 2018; PMID: 29547120		https://github.com/ekatrukha/radialitymap
Software, algorithm	MetaMorph	Molecular Devices	RRID:SCR_002368	
Software, algorithm	Leica Application Suite X	Leica Microsystems	RRID:SCR_013673	
Software, algorithm	Micro-Manager	https://micro-manager.org/	**RRID:SCR_016865**	
Software, algorithm	Huygens Software	Scientific Volume Imaging https://svi.nl/H	RRID:SCR_014237	Drift correction of ExM sample acquisitions

		uygensSoftware		
Software, algorithm	Imaris, version 9.5.1	Bitplane/Oxford instruments	RRID:SCR_007370	
Software, algorithm	*Cytosim*	Foethke et al., (2007), PMID: 19293826		
Software, algorithm	Python	https://www.python.org/	RRID:SCR_008394	
Software, algorithm	Seaborn	https://seaborn.pydata.org/	RRID:SCR_018132	
Software, algorithm	NumPy	https://numpy.org/	RRID:SCR_008633	
Software, algorithm	Pandas	https://pandas.pydata.org/	RRID:SCR_018214	
Software, algorithm	Adobe Illustrator	Adobe	RRID:SCR_010279	Generation of cartoons and figures
Other	8-well Chambered Coverglass w/ non-removable wells	Thermo	Cat# 155409	
Other	Precision cover glasses thickness No. 1.5H	Marienfeld	Cat# 0107032	Specific for ExM and STED samples

Other	silicone mold, 13mm inner diameter	Sigma-Aldrich	Cat# GBL664107	
Other	Phalloidin-Alexa488	Life Technologies	Cat# 12379	IF (1:400)
Other	Phalloidin-Alexa594	Life Technologies	Cat# 12381	IF (1:400)
Other	DAPI-containing Vectashield mounting medium	Vector Laboratories	Cat# H-1200-10	
Other	Vectashield mounting medium	Vector Laboratories	Cat# H-1000-10	
Other	Prolong Gold	Thermo Fisher	Cat# P10144	

Figure1_Hooikaas-Damstra et al. 2020

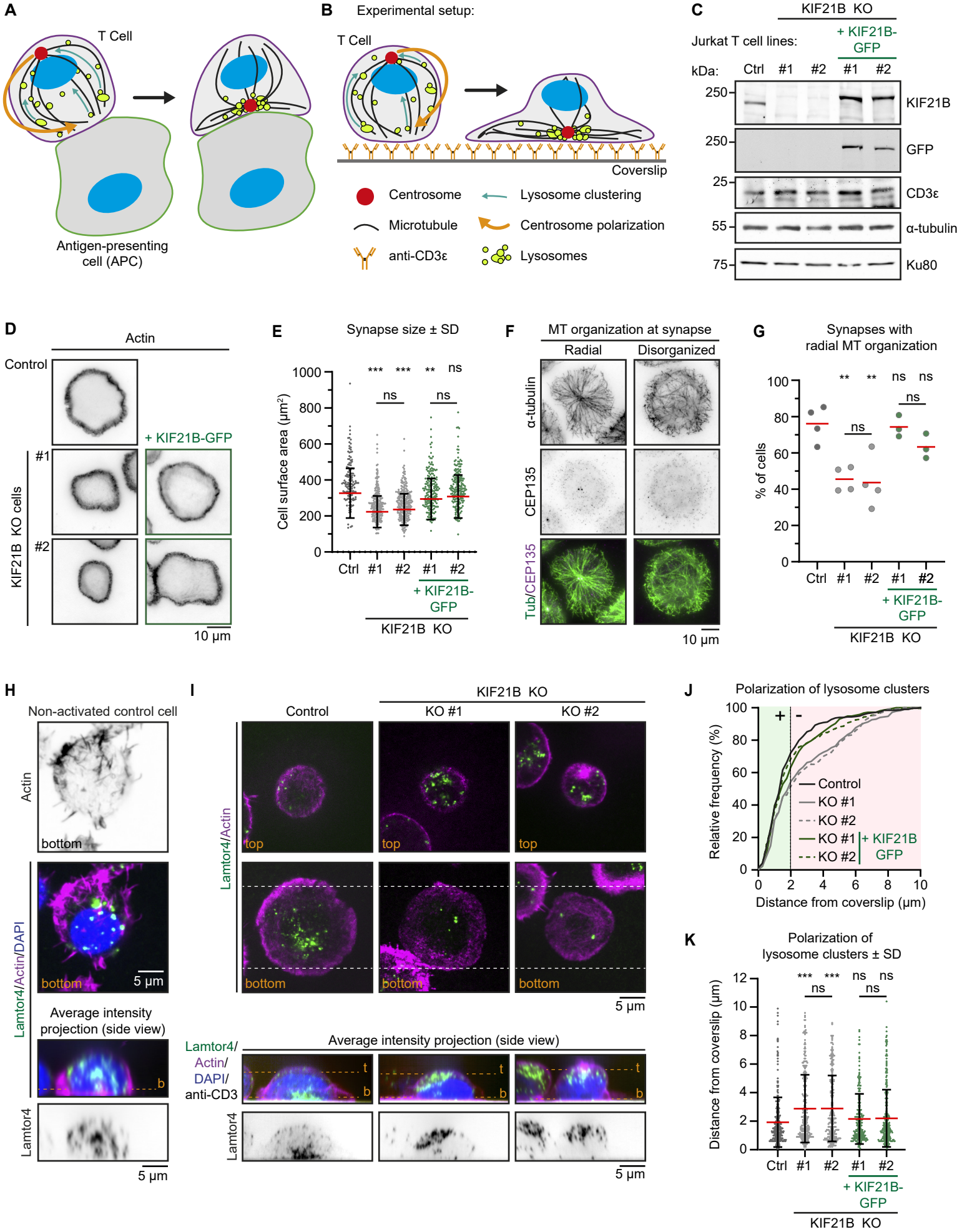

Figure2_Hooikaas-Damstra et al. 2020

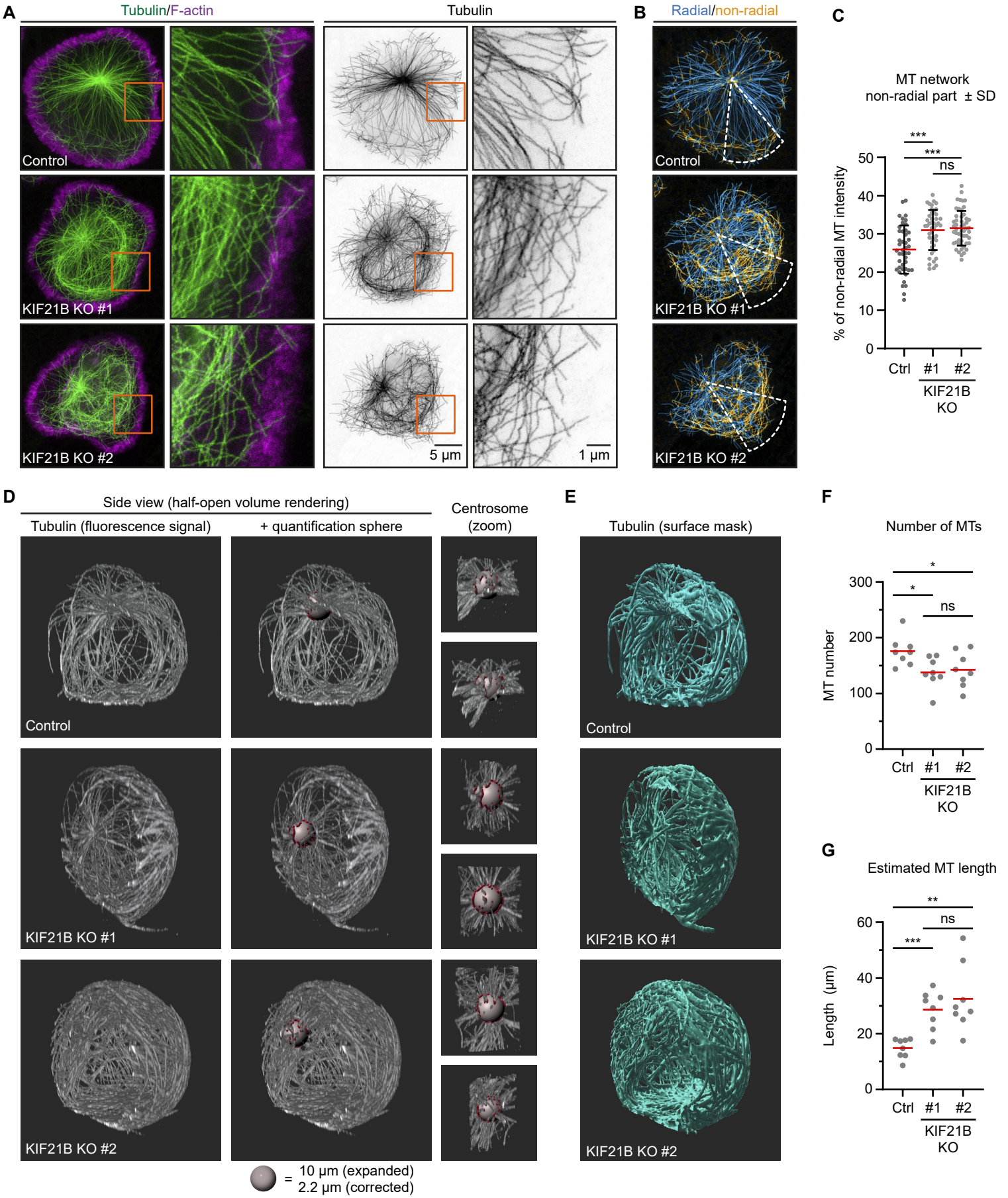

Figure3_Hooikaas-Damstra et al. 2020

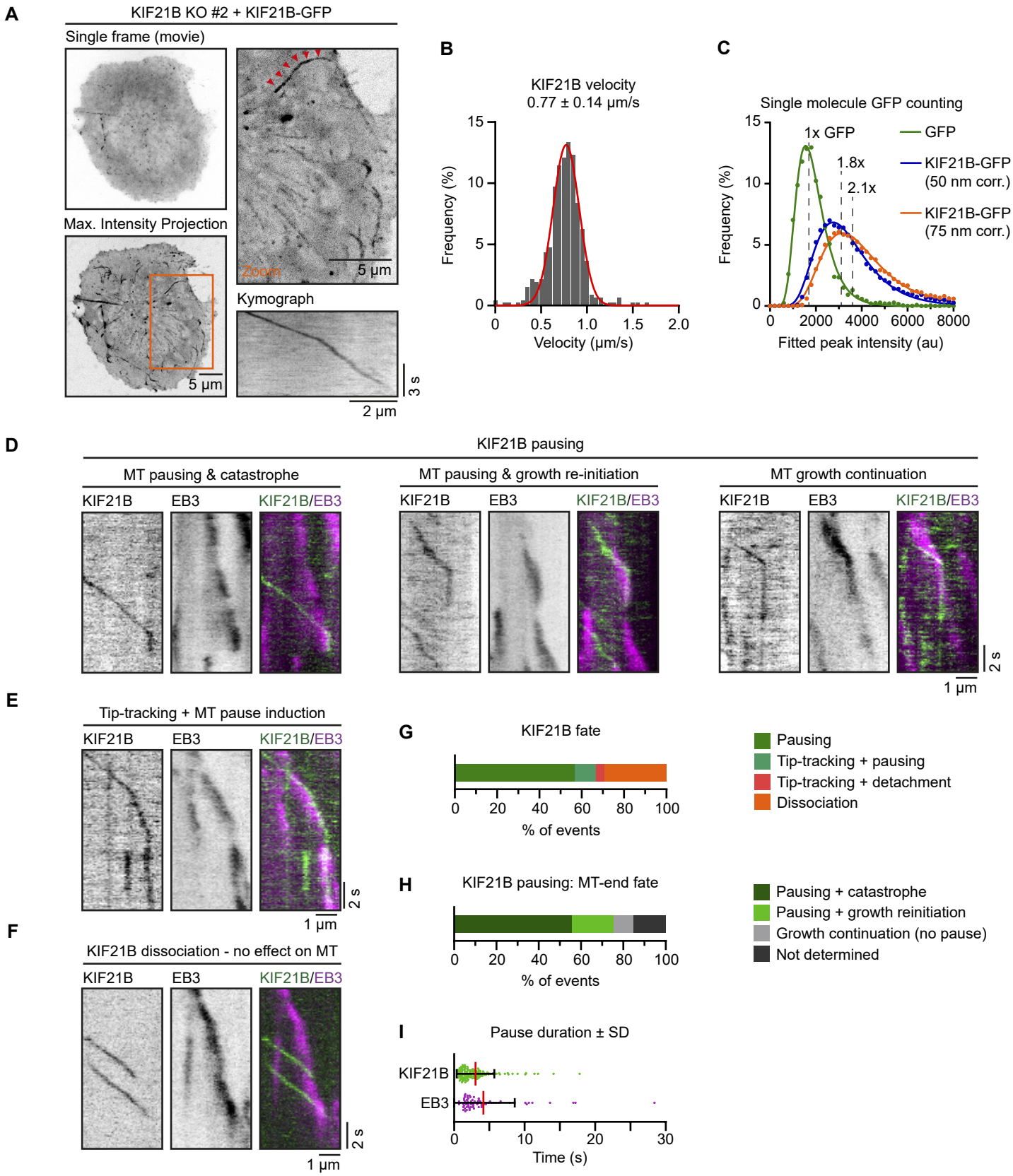

Figure4_Hooikaas-Damstra et al. 2020

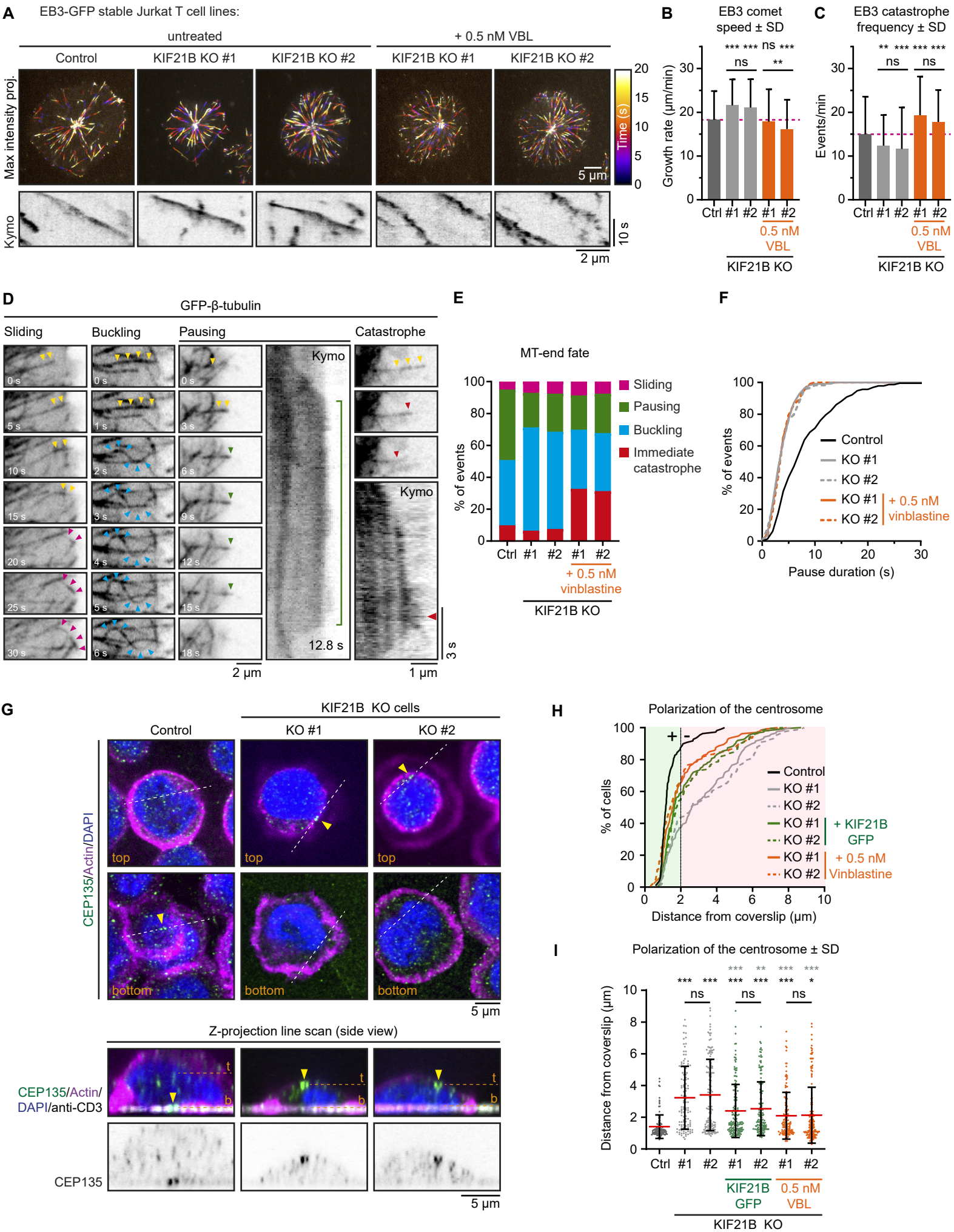

Figure5_Hooikaas-Damstra et al. 2020

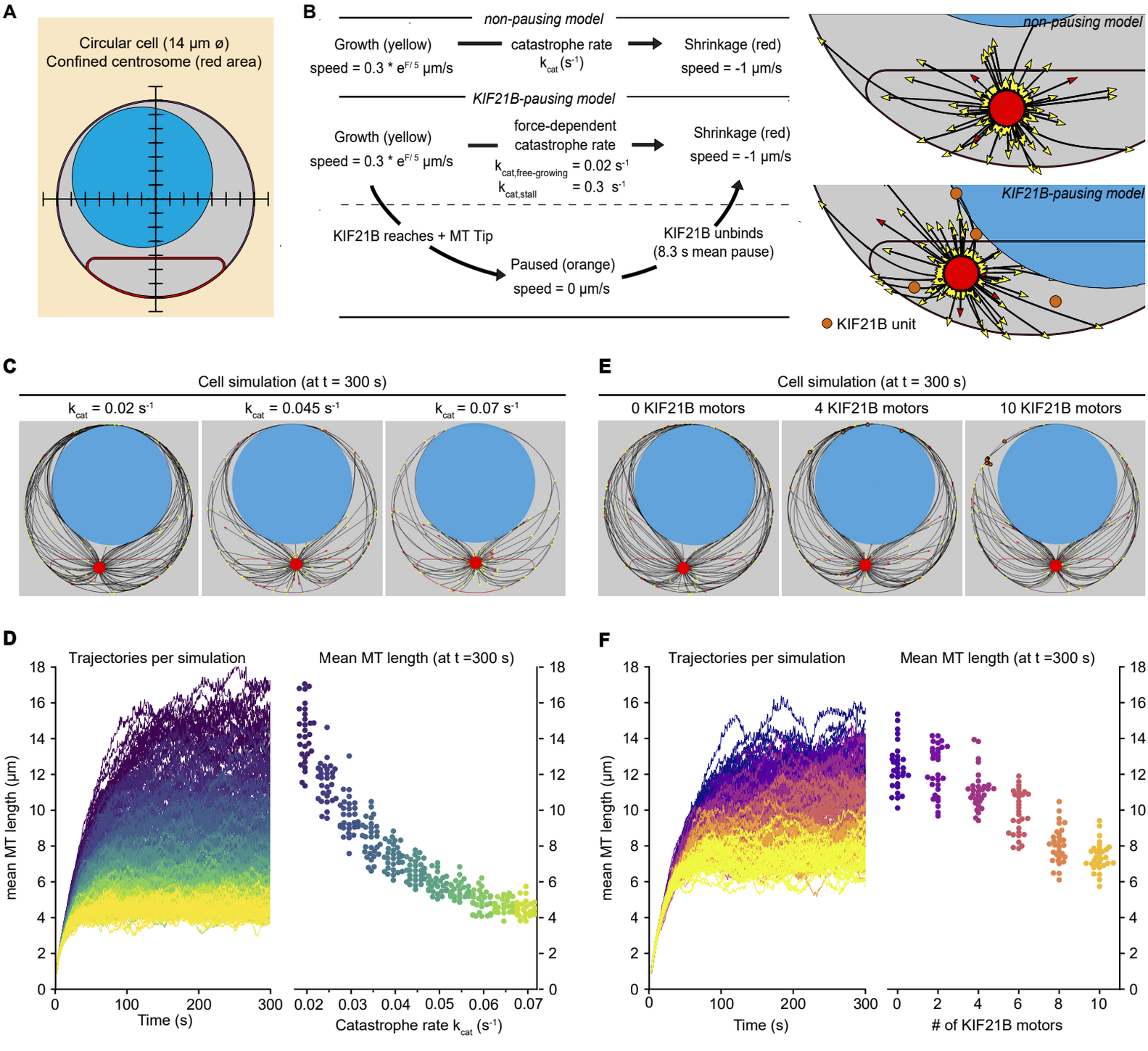

Figure6_Hooikaas-Damstra et al. 2020

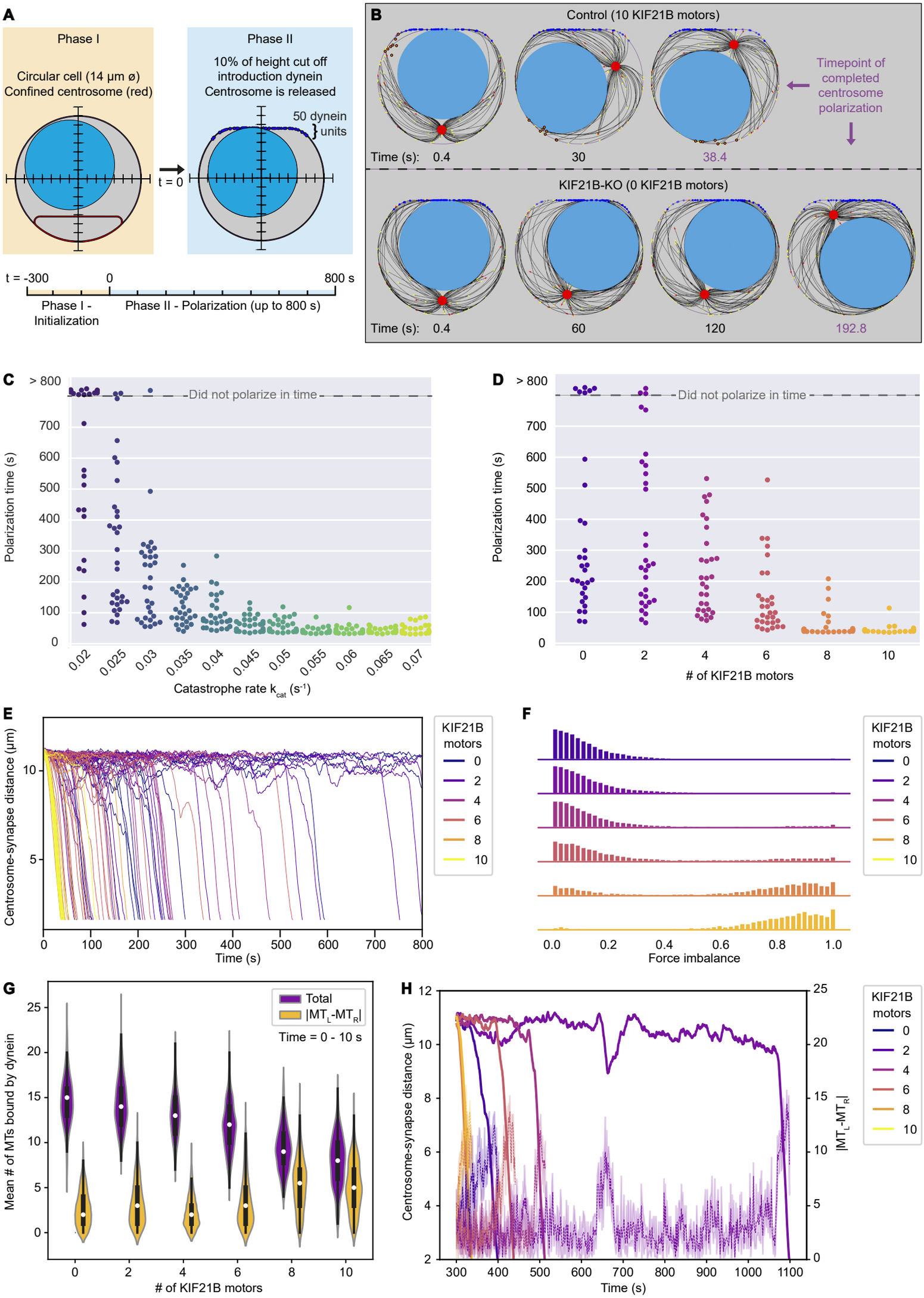

Figure7_Hooikaas-Damstra et al. 2020

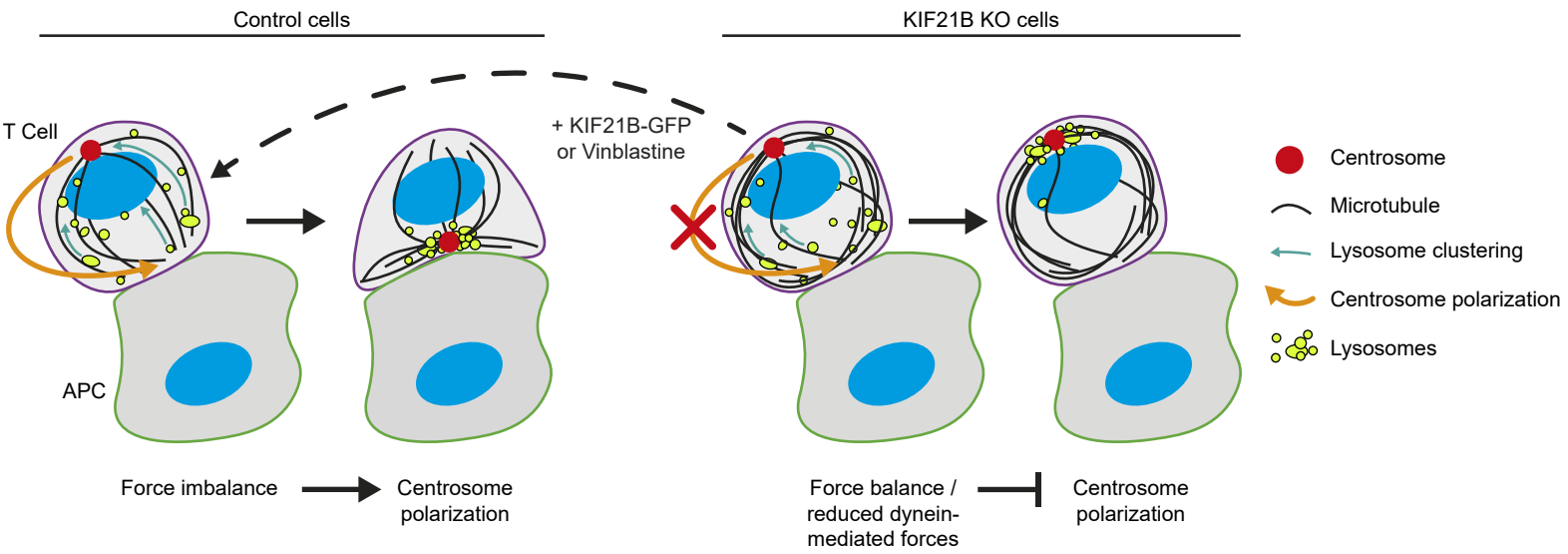

Figure 1 - Figure supplement 1_Hooikaas-Damstra et al. 2020

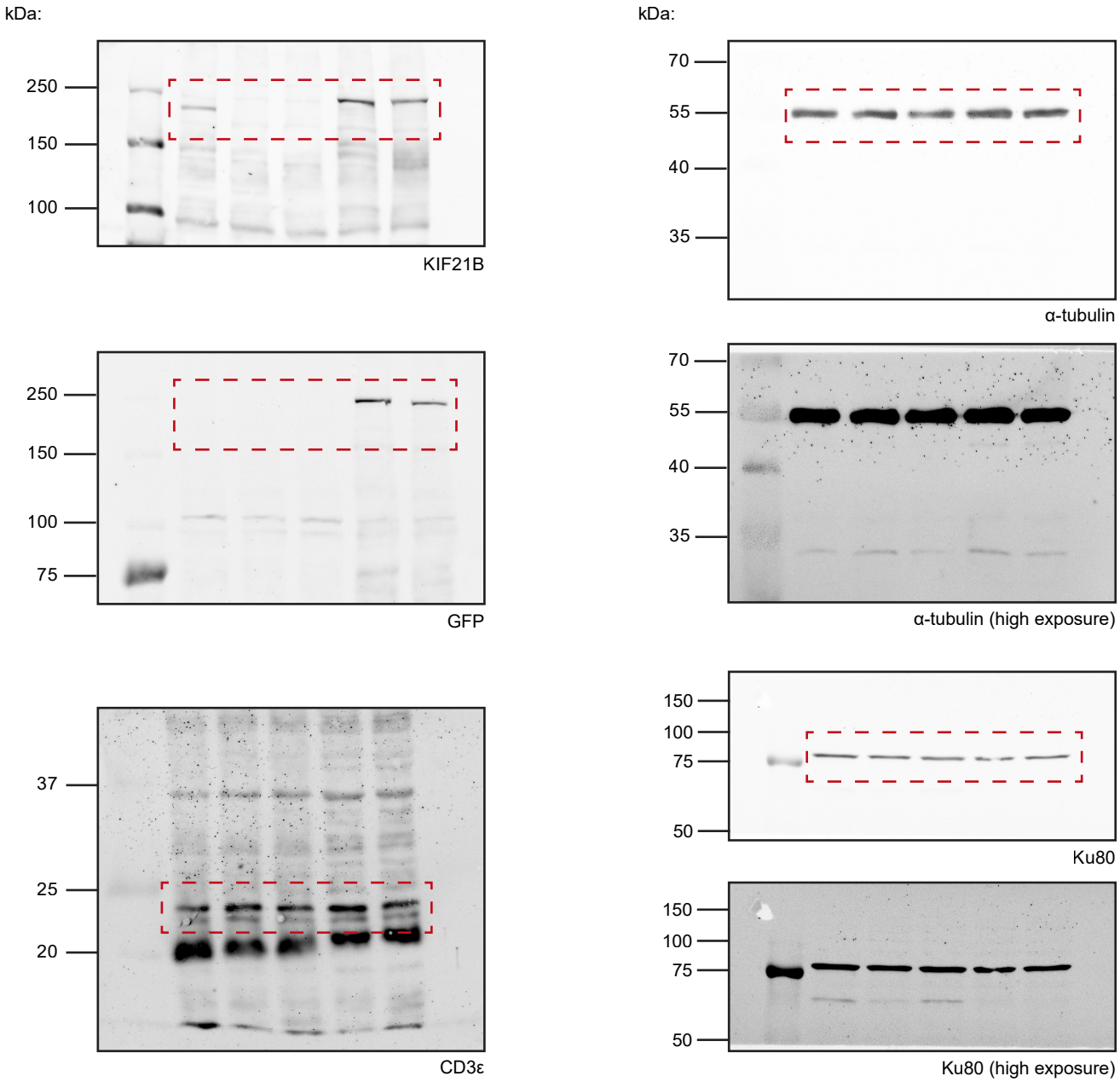

Figure 1 - figure supplement 2_Hooikaas-Damstra et al. 2020

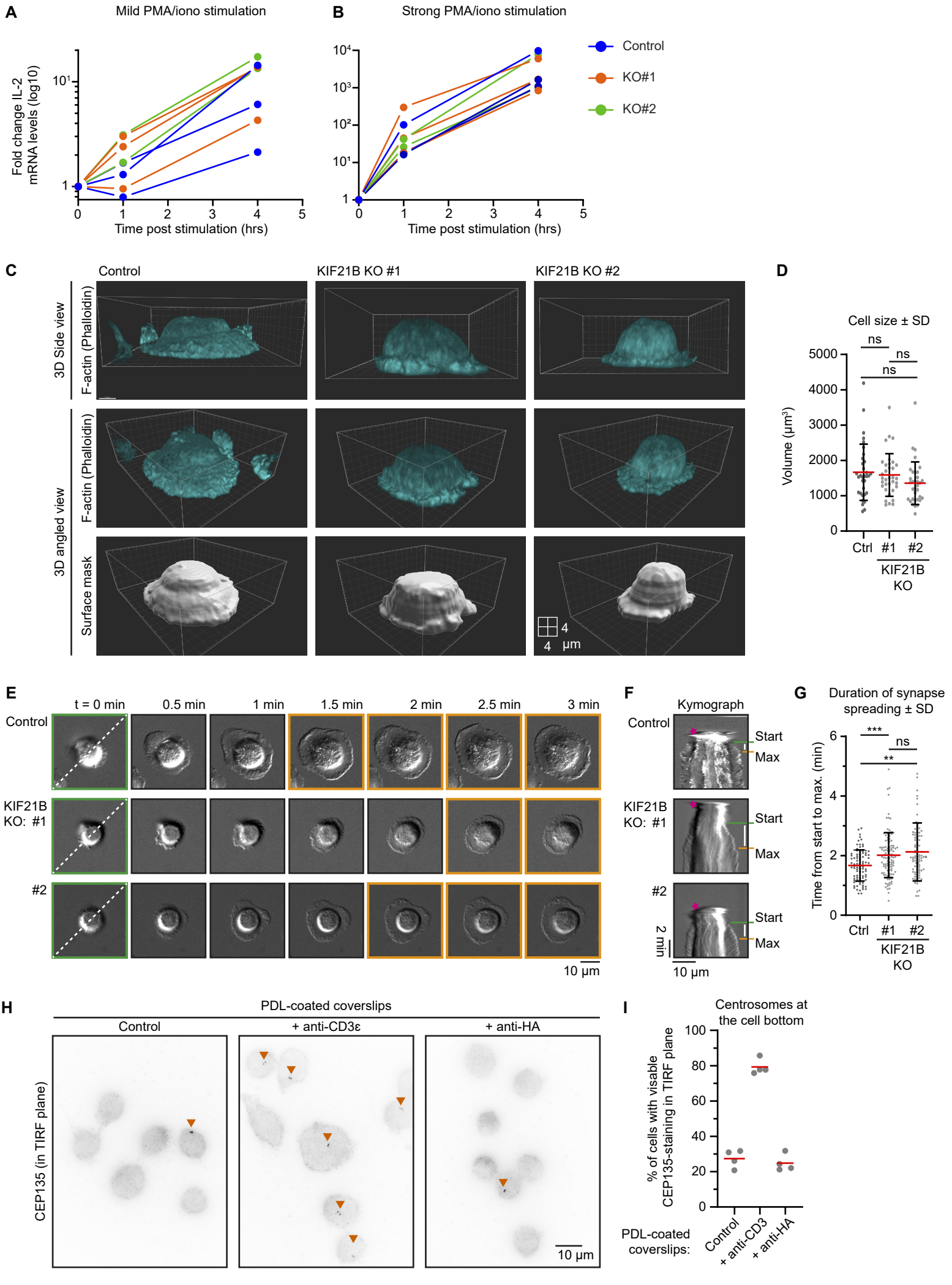

Figure 2 - figure supplement 1_Hooikaas-Damstra et al. 2020

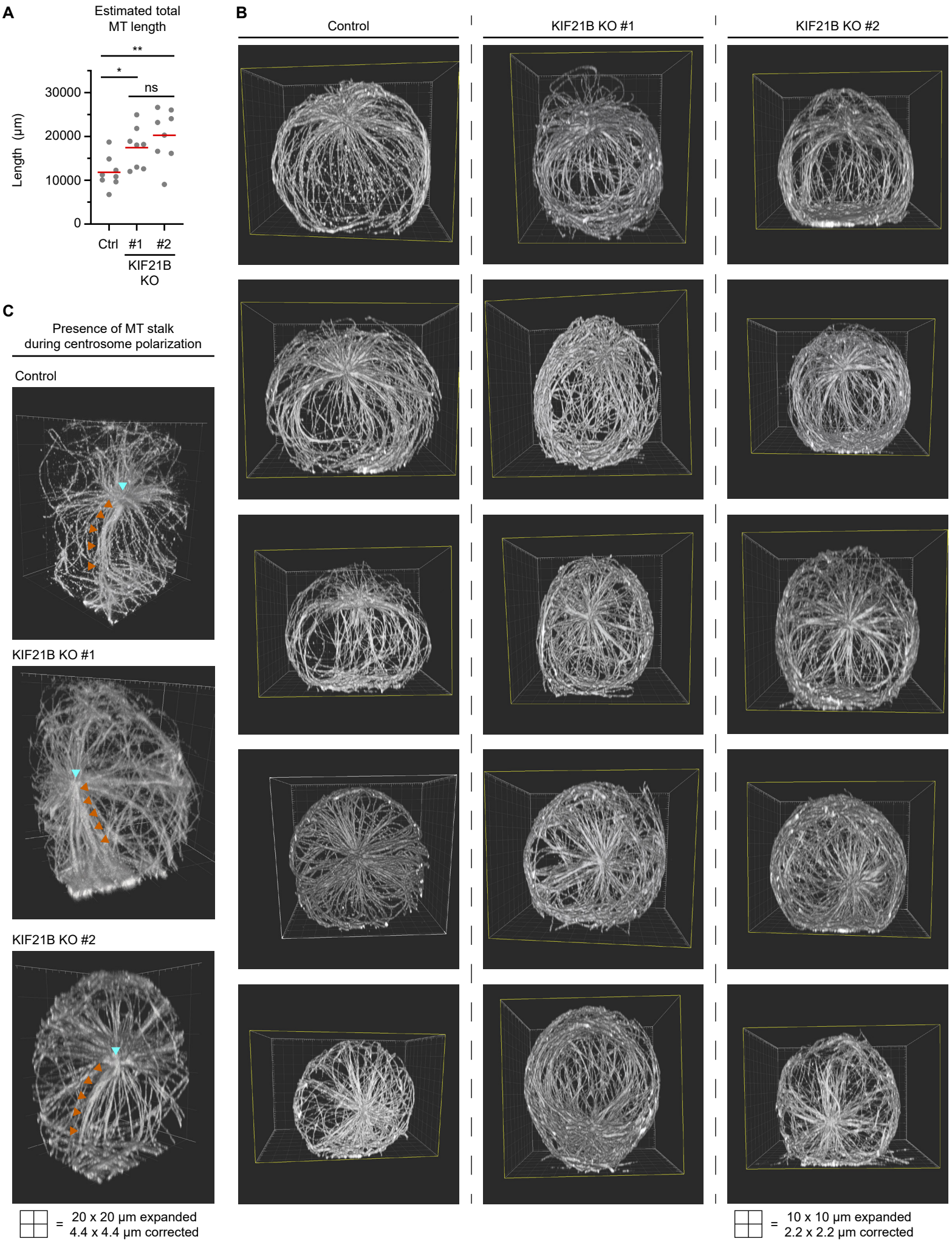

Figure 3 - figure supplement 1_Hooikaas-Damstra et al. 2020

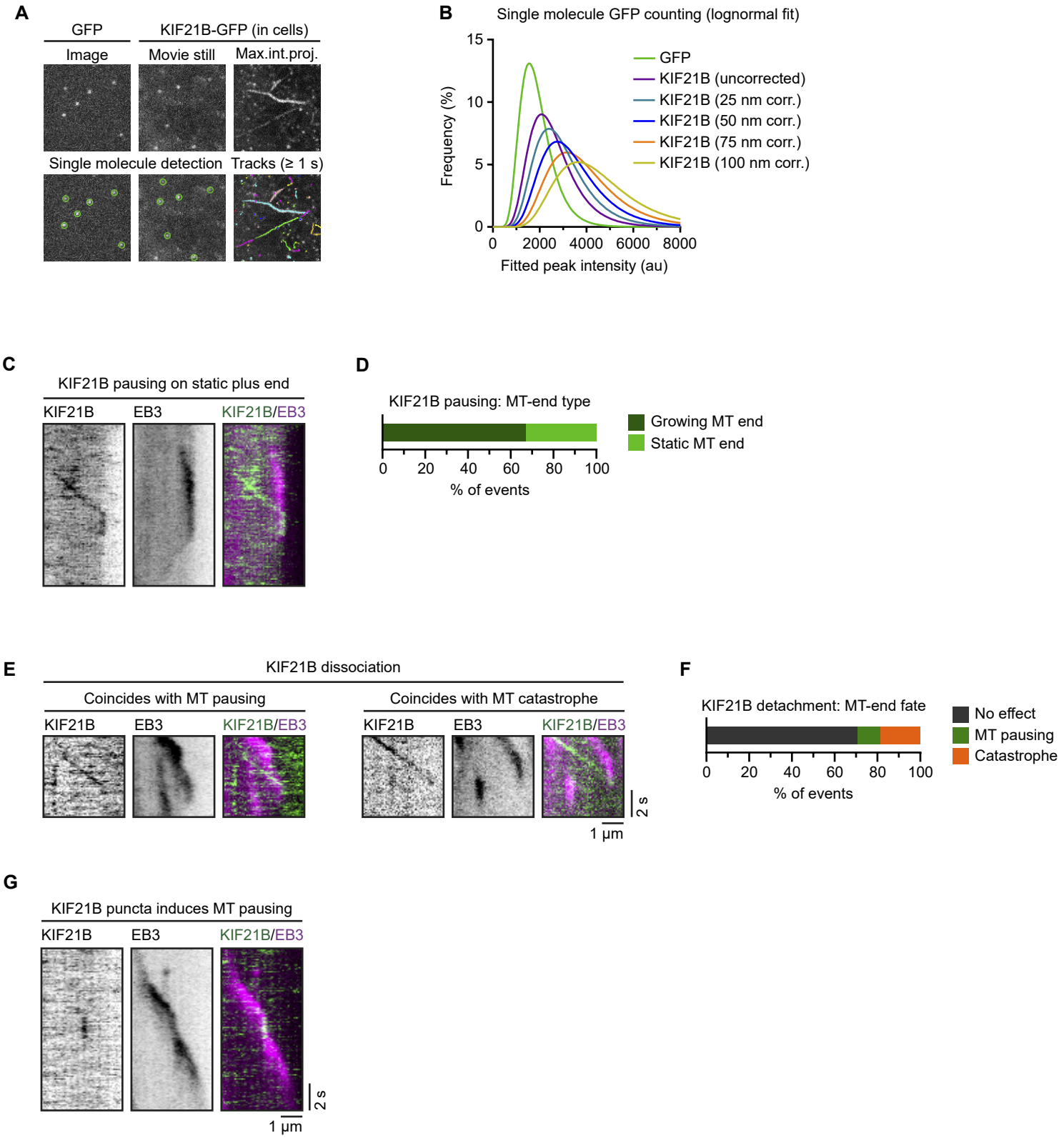

Figure 4 - figure supplement 1_Hooikaas-Damstra et al. 2020

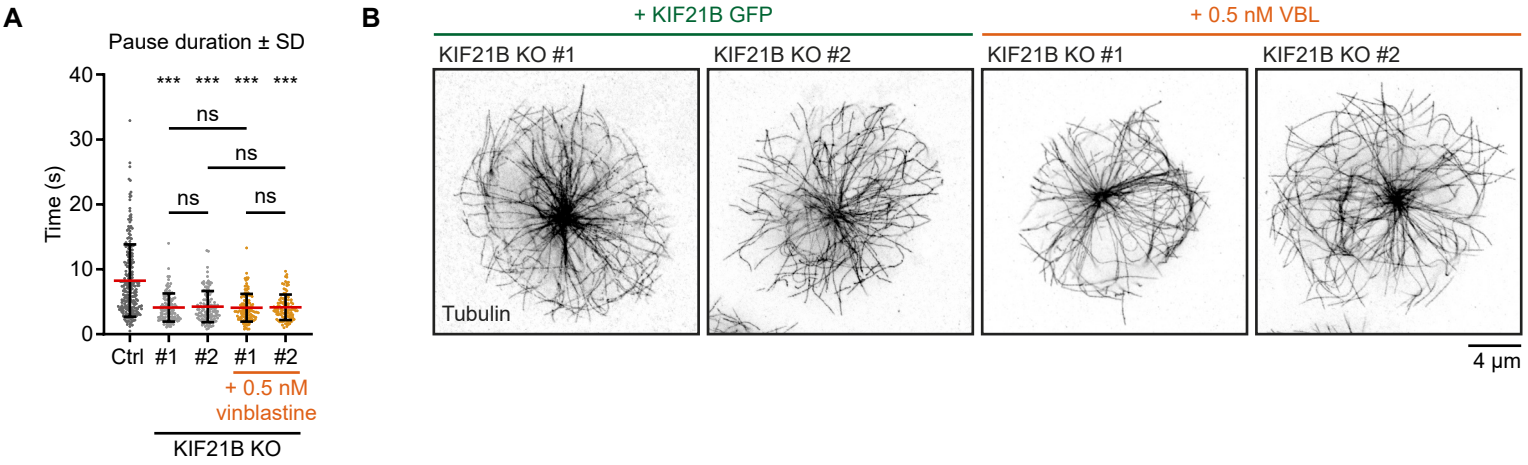

Figure 5 - figure supplement 1_Hooikaas-Damstra et al. 2020

A

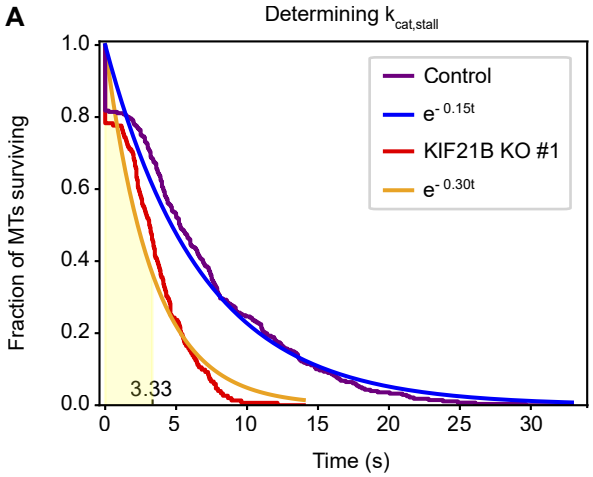

B

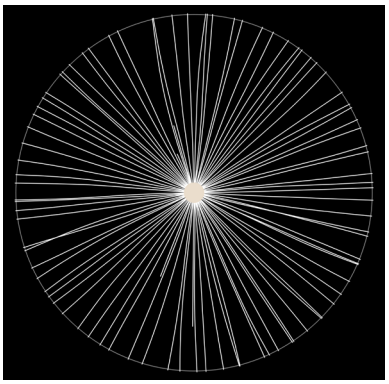

	Buckling + Sliding	Catastrophe + Pausing
Control	45.9 %	54.1 %
KIF21B KO #1	71.9 %	28.1 %
KIF21B KO #2	68.6 %	31.4 %
Mean	70.2 %	29.8 %

$$\int_0^{3.33} e^{-0.3t}dt \approx \int_0^{\tau} e^{-\frac{t}{\tau}}dt \approx 0.63$$

$$0.63 * 30 = 19\ \%\ catastrophe\ (< 3.33\ s)$$

$$100 - 19 = 81\ \%\ survive\ (< 3.33\ s)$$

C

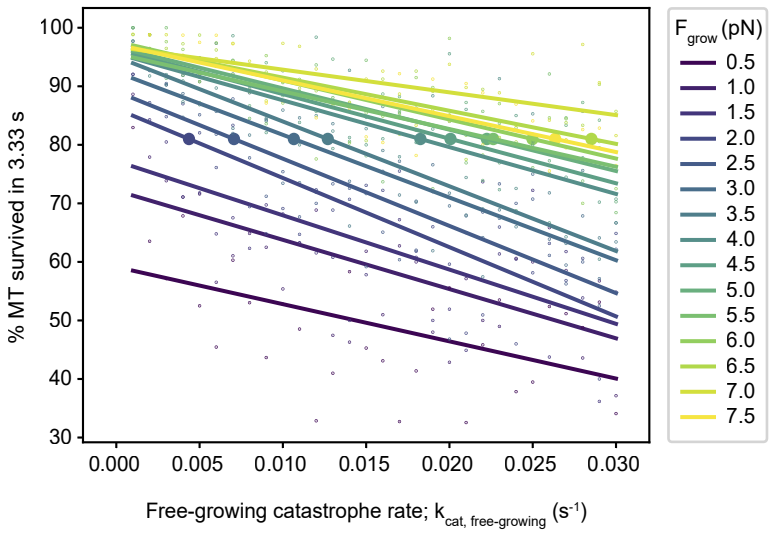

D

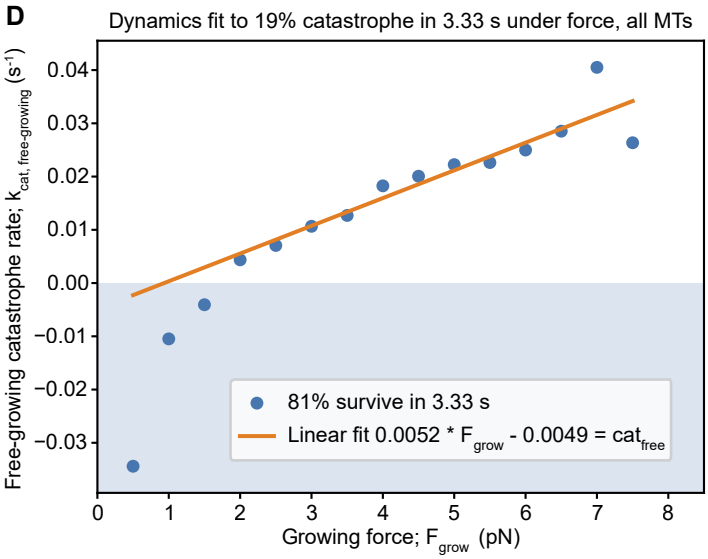
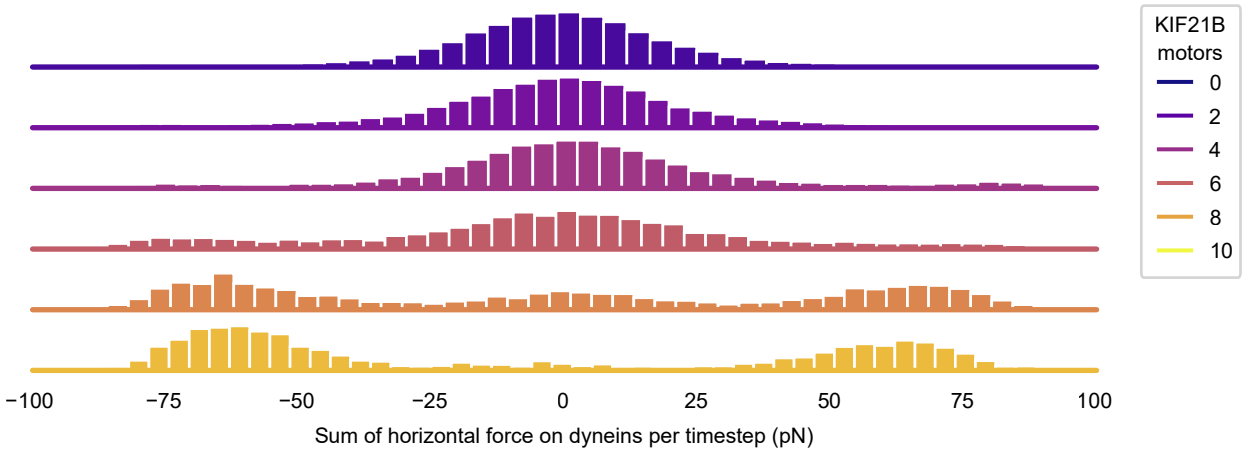
Figure 6 - figure supplement 1_Hooikaas-Damstra et al. 2020